

Chapter 3

In situ Energy Dispersive X-ray Diffraction Study: Converting Layered and Framework Ytterbium Hydroxide Phases

3.0 Introduction

From previous experiments described in Chapter 2, it was observed that the layered hydroxynitrates containing Yb and Lu were not synthesised phase pure, in both cases a second phase displaying a slightly larger interlayer separation of approximately 9.4 Å is apparent in the powder XRD data as shown in Figure 1 for $\text{Yb}_2(\text{OH})_5\text{NO}_3 \cdot x\text{H}_2\text{O}$.

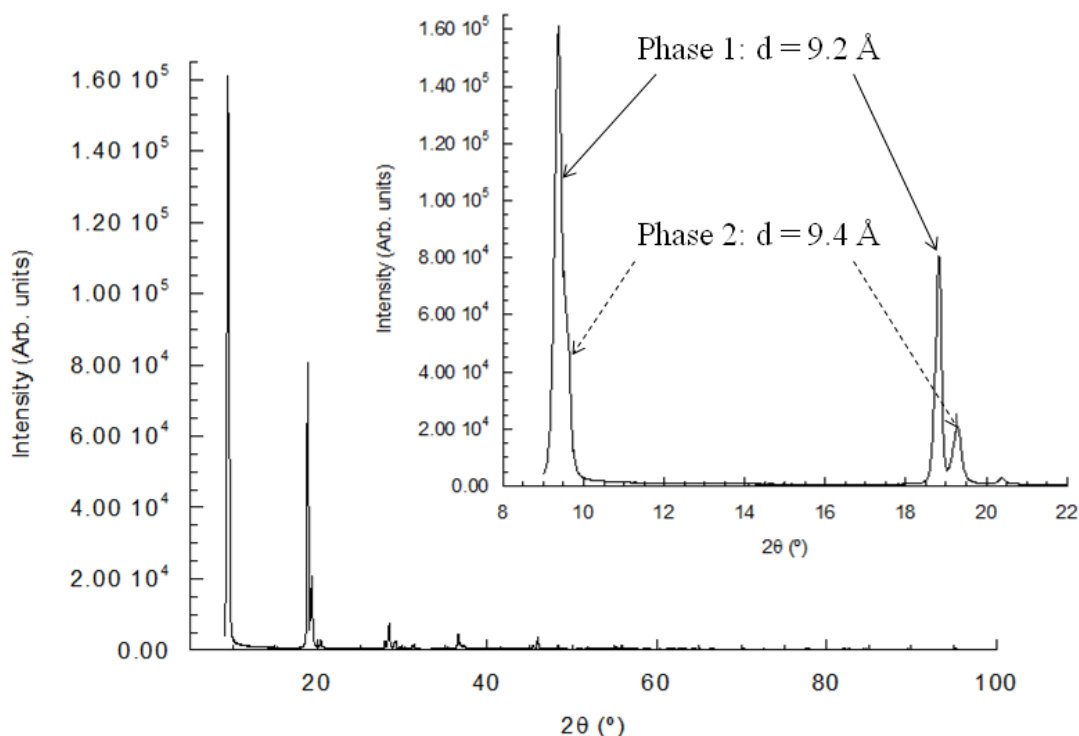


Figure 1 Powder X-ray diffraction pattern of $\text{Yb}_2(\text{OH})_5\text{NO}_3 \cdot x\text{H}_2\text{O}$ showing two layered phases with interlayer separations of 9.44 Å and 9.22 Å. INSET Enlarged diffraction pattern covering the 2θ range 9 - 22 °.

Analysis of the bulk material via TGA and elemental analysis indicates that both the Yb and Lu phases have similar compositions to the pure $\text{Ln}_2(\text{OH})_5\text{NO}_3 \cdot 1.5\text{H}_2\text{O}$ materials,

and are therefore different from the related phases reported by Haschke.¹ Analysis for the Lu material gives Lu 65.88 %, N 2.62 % and H 1.47 % (calculated for $\text{Lu}_2(\text{OH})_5\text{NO}_3 \cdot 1.5\text{H}_2\text{O}$; Lu 66.78 %, N 2.67 % and H 1.54 %) and for the Yb material gives Yb 57.61 %, N 2.28%, H 1.45 % and C 0.71 % indicating carbonate contamination (calculated for $\text{Yb}_2(\text{OH})_5\text{NO}_3 \cdot 1.5\text{H}_2\text{O}$; Yb 66.66 %, N 2.68 % and H 1.54 %).

The TGA data for $\text{Yb}_2(\text{OH})_5\text{NO}_3 \cdot x\text{H}_2\text{O}$ is shown in Figure 2 and displays three distinct mass losses comparable to those seen for other layered hydroxides. The first mass loss of 6.28 % (calculated values; $x = 1.5$ gives 5.18 % and $x = 2$ gives 6.78 %) below 150 °C corresponds to the loss of co-intercalated H_2O . The second mass loss of 6.73 % (7.28 %) by 350 °C corresponds to partial decomposition of the layers leaving a material of nominal composition ' $\text{Yb}_2\text{O}_2(\text{OH})\text{NO}_3$ '.² By 650 °C final decomposition to Yb_2O_3 is complete with a mass loss of 12.33 % (13.73 %). No further mass loss is observed above 650 °C.

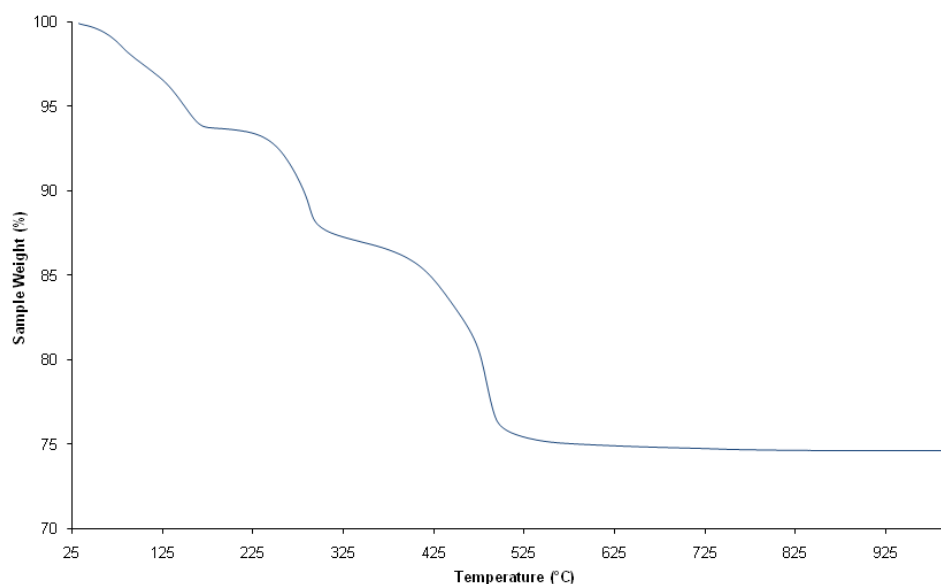


Figure 2 TGA trace for $\text{Yb}_2(\text{OH})_5\text{NO}_3 \cdot x\text{H}_2\text{O}$ showing mass losses of 6.28 % below 150 °C and further mass losses of 6.73 % by 350 °C and 12.33 % by 650 °C.

The analysis of the Yb and Lu hydroxynitrate phases by TGA and elemental analysis is broadly consistent with formula, $\text{Ln}_2(\text{OH})_5\text{NO}_3 \cdot 1.5\text{H}_2\text{O}$, suggesting that the 9.4 Å and 9.2 Å phases have a similar composition.

Extensive reaction condition screening proved unsuccessful as a means of separating these phases and so further investigations were carried out using time-resolved energy dispersive X-ray diffraction (EDXRD) at Station 16.4 of the U.K. SRS, Daresbury Laboratory.

3.1 Energy-dispersive Diffraction

The fundamental nature of the hydrothermal technique means that there is little knowledge of reaction kinetics and nucleation and growth mechanisms, with the choice of synthetic conditions often being decisive in the resulting phase formation. By performing investigations *in situ* under standard laboratory conditions, the need to continuously quench and workup reactions is removed along with the concerns that such practices raise. A non-invasive probe is required to gain further information, this probe must be powerful enough to penetrate reaction vessels and employ short collection times in order to facilitate kinetic analysis. For these reasons energy-dispersive X-ray diffraction is considered to be a suitable tool for *in situ* investigations.³

As the experiments are continuously monitored, a greater amount of detailed kinetic and mechanistic data can be collected. In energy-dispersive diffraction Bragg reflections are separated by their energy and as such, simultaneous observation of a wide range of d-spacings is possible through the use of an energy-discriminating detector positioned at a fixed angle to a white synchrotron X-ray beam. This allows the real-time monitoring of starting materials transforming to intermediate phases and the final product. As collection times can be as short as 10 s, the change in intensity of Bragg reflections can be monitored as a function of time. This is well within the reaction time for crystallisation and so it is thought that this method can shed light on the processes occurring for the biphasic products.⁴

Time-resolved, *in situ* X-ray diffraction at Station 16.4 of the U.K. SRS, Daresbury Laboratory⁵ has been previously used in the investigations of a wide range of phenomena, including the formation of second-stage intermediates in anion-exchange

reactions,⁶ the kinetic analysis of rates of intercalation into layered dichalcogenides,⁷ and the formation of an intermediate during hydrothermal syntheses.⁸

Energy-dispersive X-ray diffraction offers a method by which a whole spectrum may be measured simultaneously and rapidly, thus allowing the study of kinetics involved in phase transitions. Conventional powder diffraction uses a monochromatic beam of X-rays with known wavelength, the diffraction angle is varied in order to sample a range of lattice planes and measure their d-spacing according to Bragg's Law (Equation 1).

$$\lambda = 2d \sin \theta$$

Equation 1

Whereas in energy-dispersive diffraction, the diffraction angle is fixed and a 'white' or polychromatic beam is used. With each lattice plane diffracting X-rays of different energies. Thus we can combine Bragg's Law with Planck's relation;

$$E = h\nu = \frac{hc}{\lambda}$$

Equation 2

and substitute in the fundamental constants h and c , to give;

$$E = \frac{hc}{2d \sin \theta} = \frac{6.11926}{2d \sin \theta}$$

Equation 3

Where the units of d and E are Å and keV respectively. Diffracted X-rays are detected by a semi-conductor detector; this in turn produces a current pulse with magnitude dependant on photon energy for which the detector angle is optimized. For time-resolved studies, the high X-ray flux from synchrotron source is required.

3.2 Apparatus

Time-resolved *in situ* energy dispersive X-ray diffraction experiments were carried out at Station 16.4 of the UK SRS.⁹⁻¹¹ The UK SRS (Figure 3) is a low emittance storage ring operated at 2 GeV with stored beam currents in excess of 200 mA. The radiation is emitted from 2 poles of a superconducting wiggler magnet with a peak field of 5 T. The useful flux falls in the range 5 – 80 keV (peak of 7×10^{11} photons/s/mm² in 0.1 % bandwidth at 10 keV). The polychromatic beam is refined by a tungsten-carbide collimator to a diameter of 0.5 mm. A multi-slit system is used to define the diffraction angle. This system consists of 50 slits (400 x 0.5 mm stainless steel foils) held 0.1 mm apart. This allows the acceptance angle to be well matched to the detector resolution. The detector is an intrinsic Ge solid state detector.



Figure 3 UK Synchrotron Radiation Source, Daresbury Laboratory.

Multi-slit EDXRD can be used to study reactions *in situ* at temperature and pressure, with a timescale for collection of the order of 10 seconds.¹² A schematic diagram to show the detector arrangement of Station 16.4 is shown in Figure 4 and the experimental setup is shown in Figure 5.

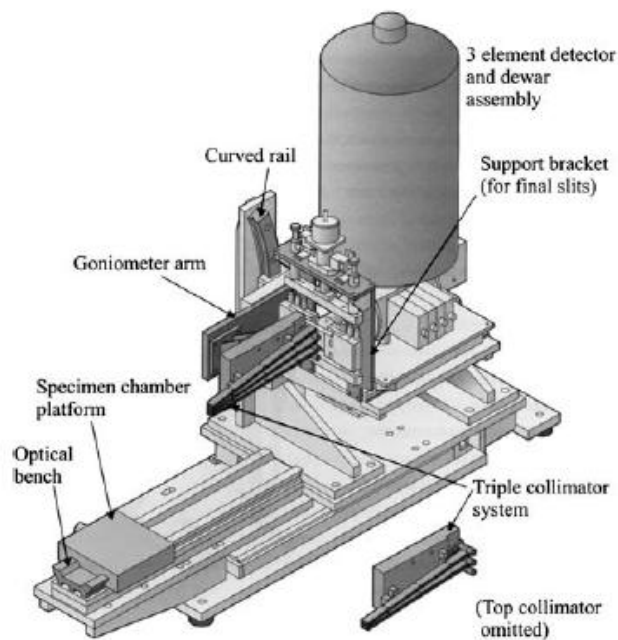


Figure 4 Schematic representation of the detector arrangement at Station 16.4 of the UK SRS.⁴

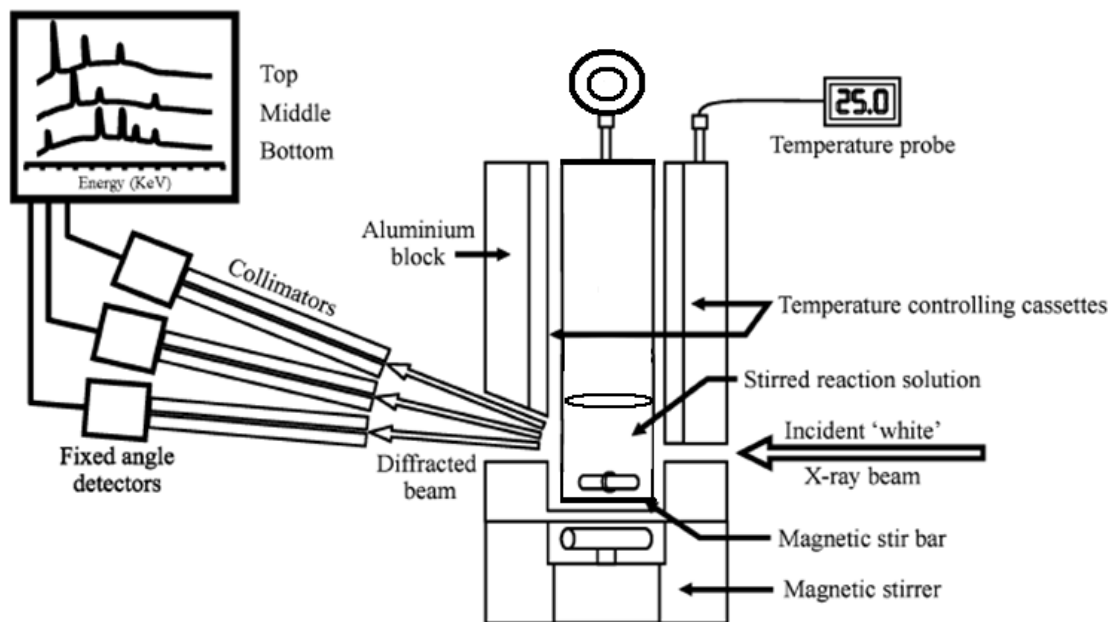


Figure 5 Schematic diagram to show experimental setup at Station 16.4 (adapted from *Chem. Mater.* 2000, **16**, 975).¹³

The apparatus is secured on an optical bench. To allow maximum diffracted intensity, the rig can be moved, thus obtaining the ideal alignment of the diffraction lozenge with

the sample. The solid state detector is positioned by a series of motors to the required angle. The reaction cell consists of a solid aluminium block heating jacket with lid, within which is a hydrothermal reaction vessel or Pyrex quickfit flask. The temperature of the block is maintained by a system of electric cartridge heaters and temperatures can be selected from room temperature to 230 °C. The base of the jacket is thinned to allow external magnetic stirring. The hydrothermal reaction vessel, shown in Figure 6, is stainless steel with PTFE lining. A bursting disc assembly is fitted for safety purposes and a pressure transducer displays the pressure inside the cell. The 95 mm long cell, 24.33 mm in diameter has an internal volume of 44 cm³ and is capable of operation at pressures up to 600 psi. The PTFE liner of volume 30 cm³ is operational to temperatures of 230 °C. The stainless steel cell walls are 3 mm thick, thinned down to 1 mm at the base to allow the beam to pass through.



Figure 6 Hydrothermal cell used in experiments.

The reaction mixtures are stirred to ensure that sufficient solid remains in the beam. Stirring is achieved by means of a magnetic stirrer mounted at the base of the block. The maximum count rate is limited by the detector and counting chain to approximately $\sim 5 \times 10^4$ count/s.⁹

3.3 Solid-State Kinetics

Solid state kinetics is governed by the breaking and forming of bonds as well as the transport of matter to the reaction zone. Generally kinetic analysis takes the form,

$$F(\alpha) = kt$$

Equation 4

Where α is the extent of reaction, k is the rate constant and t is the reaction time.

For the purposes of extracting kinetic data, the Bragg reflection of interest is integrated according to a Gaussian fitting regime and the maximum intensity (I_{max}) of the reflection is used to ascertain the extent of reaction from 0 to 1 at time, t according to Equation 5.

$$\alpha(t) = \frac{I(t)}{I_{max}}$$

Equation 5

Extent of reaction curves ($\alpha(t)$ vs. t) provide a simple means by which induction times can be compared and, where a number of systems are studied under the same conditions, the repetition of characteristic curve shapes can highlight similarities in nucleation mechanisms.

A number of kinetic expressions can be derived from $F(\alpha)$ for different nucleation mechanisms, depending on whether the reaction is diffusion-controlled, reaction rate-controlled or displays first order kinetics.¹⁴ The most commonly used equations are summarised below in Table 1.⁸

Table 1 Useful forms of the common rate equations used to model solid-state reactions.⁸

Growth model	Equation
Acceleratory rate	
Power law	$\alpha^{\frac{1}{n}} = kt$
Sigmoidal rate	
Avrami-Erofe'ev	
<i>First order</i>	$[\ln(1 - \alpha)] = kt$
<i>Second order</i>	$[\ln(1 - \alpha)]^{\frac{1}{2}} = kt$
<i>Third order</i>	$[\ln(1 - \alpha)]^{\frac{1}{3}} = kt$
<i>Fourth order</i>	$[\ln(1 - \alpha)]^{\frac{1}{4}} = kt$
Prout-Tomkins	$\ln\left[\frac{\alpha}{1 - \alpha}\right] = kt$
Deceleratory rate	
1-D diffusion	$\alpha^2 = kt$
2-D diffusion	$(1 - \alpha) \ln(1 - \alpha) + \alpha = kt$
3-D diffusion	$\left[1 - (1 - \alpha)^{\frac{1}{3}}\right]^2 = kt$
Ginstling-Brounshtein	$1 - \frac{2\alpha}{3} - (1 - \alpha)^{\frac{2}{3}} = kt$
Contracting area	$1 - (1 - \alpha)^{\frac{1}{2}} = kt$
Contracting volume	$1 - (1 - \alpha)^{\frac{1}{3}} = kt$

3.3.1 Avrami-Erofe'ev

The Avrami-Erofe'ev expression is the most commonly used model in the treatment of solid state kinetic data.¹⁵⁻¹⁸ The model has previously been applied to a range of processes including intercalation,^{13, 19} phase transformations,²⁰ and the crystallisation of zeolites.²¹

The relationship takes into account that nucleation may be a random process, not followed by rapid growth (as nuclei grow they must eventually touch so that further growth is prevented) and so assumes that the reaction proceeds via separate stages of nucleation and growth.¹⁴ The relationship can be expressed as;

$$-\ln(1 - \alpha) = [k(t - t_0)]^n$$

Equation 6

Where t is the reaction time, t_0 is the induction time, n is the exponent and k is the rate constant. Hulbert has evaluated the exponent under a range of conditions and shown that the exponent value can be used to determine the rate of nucleation and dimension of growth of the nuclei, summarised below in Table 2.^{4, 22}

The Avrami exponent, in favourable cases can be used to ascertain whether a reaction is phase-boundary (n) or diffusion-controlled (m). The exponent is also indicative of the number of steps involved in nucleation of the product, β and λ , the number of dimensions in which the nuclei grow. Nucleation may be instantaneous ($\beta = 0$), constant ($\beta = 1$) or deceleratory ($0 < \beta < 1$), with growth in one to three dimensions ($\lambda = 1 - 3$). For diffusion-controlled reactions $n = \beta + \lambda / 2$ and for phase boundary controlled reactions $n = \beta + \lambda$. It is, however, important to note that it can be difficult to distinguish β and λ . In addition, interpretation of these values can be difficult, and a given value does not allow the unambiguous determination of the reaction mechanism.

Table 2 Nuclei growth models for solid state reactions.⁴

Dimension of growth (λ)	Nucleation rate (β)	Exponent value	
		Phase boundary controlled (n)	Diffusion controlled (m)
1	Zero (instantaneous)	1	0.5
	Deceleratory	1-2	0.5-1.5
	Constant	2	1.5
2	Zero (instantaneous)	2	1
	Deceleratory	2-3	1-2
	Constant	3	2
3	Zero (instantaneous)	3	1.5
	Deceleratory	3-4	1.5-2.5
	Constant	4	2.5

Values for the exponent and rate constant can be obtained through the use of Sharp-Hancock plots,²³ by taking logarithms of both sides of the Avrami-Erofe'ev expression (Equation 6);

$$\ln[-\ln(1-\alpha)] = n \ln(t - t_0) + n \ln(k)$$

Equation 7

Whereby a plot of $\ln[-\ln(1-\alpha)]$ against $\ln t$ gives a straight line with gradient, n and intercept, $n \ln(k)$, thus allowing the values for the exponent and rate constant to be determined. The Sharp-Hancock plot is most applicable over the range $0.15 < \alpha < 0.85$. This plot also provides a convenient means of checking whether Avrami-Erofe'ev kinetics are an appropriate treatment for the data.

3.4 Previous Uses

Time-resolved, *in situ* X-ray diffraction at Stage 16.4 of the U.K. SRS, Daresbury Laboratory has been previously used to study a wide range of reactions, including staging in the intercalation reactions of layered double hydroxides. Fogg *et al.* studied the anion exchange reactions of the layered double hydroxide $[\text{LiAl}_2(\text{OH})_6]\text{Cl}\cdot\text{H}_2\text{O}$ with a range of aromatic and aliphatic dicarboxylates.⁶ The use of EDXRD allowed the observation of a rare example of the formation of second-stage intermediates for materials of this type. Figure 7a shows a stack plot of the EDXRD data for the reaction of the host material with disodium succinate and Figure 7b the integrated intensities of the reflections observed. Clearly visible is the immediate decay of the 001 Bragg reflection and the simultaneous growth of a reflection of d-spacing corresponding to 9.9 Å, assignable as the 002 reflection of the second stage intermediate $[\text{LiAl}_2(\text{OH})_6]_4[\text{C}_4\text{H}_4\text{O}_4]\text{Cl}_2\cdot x\text{H}_2\text{O}$ ($x \sim 7$). It is only once this intermediate has gone through its maximum that the appearance of the 001 reflection of the first stage product is observed at $d = 12.9$ Å. In this case, reaction half-lives were of the order of 1-2 minutes at room temperature and so dropwise addition of the guest via syringe pump was used to allow reaction monitoring, thus a kinetic study of the data was precluded.

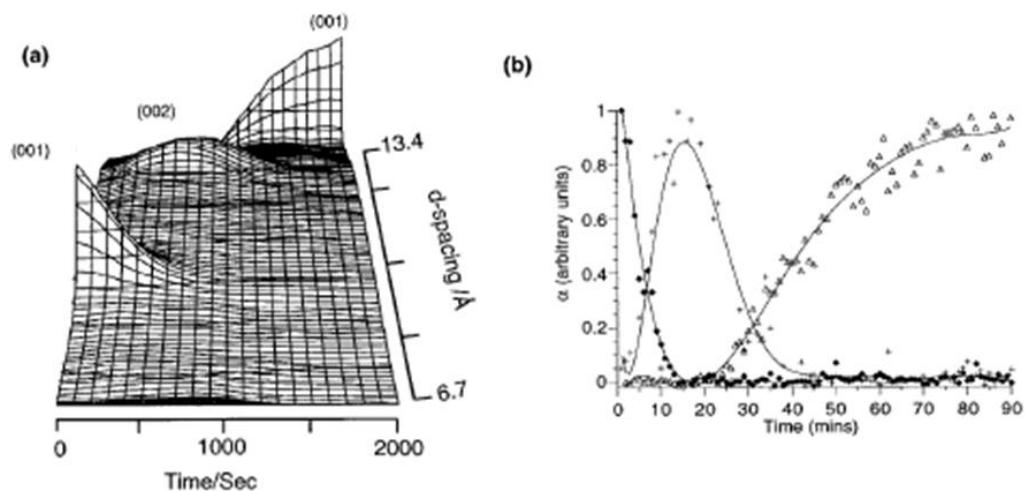


Figure 7 (a) 3D stacked plot show anion exchange reaction between $[\text{LiAl}_2(\text{OH})_6]\cdot\text{H}_2\text{O}$ and disodium succinate (b) plot of integrated intensity of (001) of the host material, (002) of the intermediate species and (001) of the final product.⁶

In situ X-ray diffraction experiments have been used to monitor the liquid-phase reconstruction of Mg-Al-carbonate hydroxalcalite like compounds.²⁴ Following calcination of MgAl LDH at 400 °C, resultant oxide was suspended in sodium carbonate solution and the reaction monitored at temperatures up to 120 °C. Bragg reflections corresponding to the reconstructed LDH were immediately apparent and reactions reached completion in under 3 hours. Reconstruction was found to occur more rapidly at elevated temperatures. Indeed particle size, as measured from the FWHM of the product Bragg reflection, increased with increasing temperature. For reactions carried out at 25 °C a particle size of 90 Å was observed. In contrast, those measured at 120 °C were 337 Å. Information concerning the mechanism of formation of the LDH was obtained using Avrami-Erofe'ev kinetics. At low temperatures the reaction is governed by the rate at which nucleation sites form. At increased temperatures, these nucleation sites form at a faster rate so that as the reaction reaches its later stages, the reaction is limited by the rate at which the reactants diffuse to the nucleation sites. This in-depth study allowed the calculation of the activation energy for the nucleation controlled crystal growth to be determined as + 41 kJ mol⁻¹.

EDXRD has also been used to perform studies on the rates of intercalation of the air-sensitive guest cobaltacene, Co(η -C₅H₅)₂ into the layered dichalcogenides, ZrS₂, 2H-SnS₂, 2H-SnSe₂, 2H-TaS₂, 2H-NbS₂, 1T-TaS₂ and TiS₂.⁷ In this extensive study, which probes the effects of temperature, host lattice, concentration and solvent the authors were able to determine the half-life of each reaction and found that the rate of intercalation is independent of initial cobaltacene concentration with no evidence of any crystalline intermediate phases. The Avrami-Erofe'ev Model when applied to the data gave best fit for $m = 1.5$, indicative of deceleratory nuclei growth. Analysis by Sharp-Hancock plot however revealed more complex behaviour. It is postulated that the reaction proceeds first with $m = 2$ and then in the later stages with $m = 1$. Further analysis for the intercalation into 2H-SnS₂ revealed that the activation energy for this reaction was 41 +/- 7 kJ mol⁻¹.

The hydrothermal synthesis of the large-pore oxy-fluorinated gallophosphate, ULM-5 under a variety of conditions has been investigated by Francis and co-workers.^{8, 25} When using orthophosphoric acid as a precursor ULM-5 is formed rapidly with the kinetics of the reaction governed by diffusion, temperature variations simply giving longer induction times. However when phosphorous pentoxide is used, the reaction is found to proceed via one of two crystalline phases with the rate being highly dependant on temperature. Figure 8 shows that after only a short period Bragg reflections indicative of a previously unknown intermediate phase begin to grow, reaching a maximum after approximately 18 minutes.

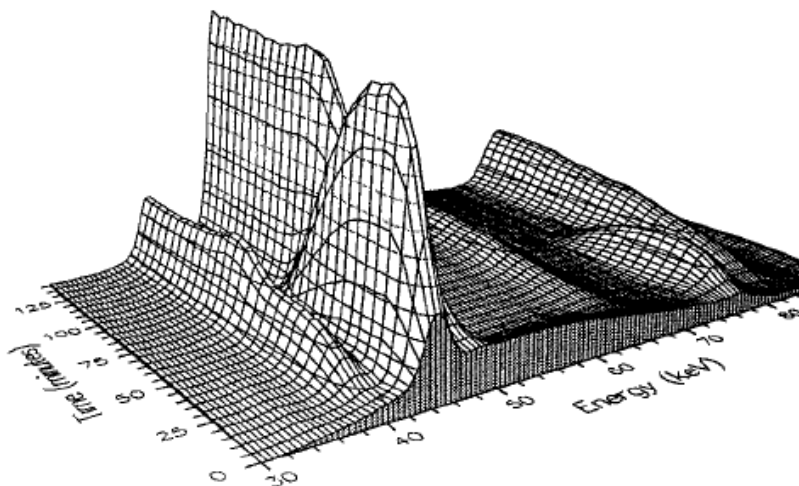


Figure 8 3D stack plot of EDXRD data for the synthesis of ULM-5 at 180 °C using P_2O_5 as starting material.

These peaks then begin to decay and diffraction peaks due to ULM-5 formation appear and increase in intensity. The reflections due to the intermediate decay very slowly, it is 70 minutes before they are completely absent from the diffraction pattern, ULM-5 reflections subsequently reach their maximum. Attempts to isolate these intermediates via *in situ* quenching procedure proved unsuccessful. It is noted that results reveal the potentially highly complex nature of hydrothermal synthesis and thus the power of this diffraction technique as a means by which such observations can be quickly and efficiently disseminated.

The hydrothermal synthesis of the closely related ULM-3 and ULM-4 structures have also been studied *in situ*.²⁶ In the investigation reagents and reaction temperature were varied, revealing a complex system with other transient intermediate phases observed. As for ULM-5 the reaction kinetics in these reactions are diffusion-controlled. Crystallisation proceeds at the same rate across the temperatures studied 140 – 200 °C, however the choice of phosphorous reagent is key, with no intermediate observed when P₂O₅ is used in the synthesis of ULM-4.

The one-dimensional fluorodiphosphate Ga(P₂O₇)F·H₃N(CH₂)₃NH₃·H₂O has since been identified as the intermediate observed in the formation of ULM-3 where P₂O₅ is used.^{27, 28} The crystallisation of this phase is preceded by the dissolution of Ga(P₂O₇)F·H₃N(CH₂)₃NH₃·3H₂O. Both structures were identified in *in situ* experiments and their structures solved from powder X-ray diffraction data.

The technique has also been used to investigate the hydrothermal crystallisation of the mesoporous silicates FSM-16 and MCM-41.^{29, 30} In this case also, choice of precursor for the reaction was found to be crucial with the silica-surfactant mesophases formed highly-dependant on the reaction medium. These materials are known for their inherent disorder and despite this and the large d-spacings a thorough and in-depth study of their behaviour was facilitated by the short acquisition times and data quality of Station 16.4.

3.5 Scope of Chapter

Here we report the findings of a time-resolved *in situ* X-ray powder diffraction study following the observation of biphasic Yb₂(OH)₅NO₃·xH₂O (d = 9.2 and 9.4 Å) when synthesised under standard laboratory conditions. Reaction temperature and metal and concentration are varied. Three different phases with the layer composition [Yb₂(OH)₅]⁺; Yb₂(OH)₅NO₃·1.5H₂O d = 9.2 Å (phase **1**), Yb₂(OH)₅NO₃·2H₂O d = 9.4 Å (phase **2**) and Yb₂(OH)₅NO₃·H₂O d = 8.5 Å (phase **3**) are apparent, which ultimately all transform to a 3D structure with d = 8.0 Å, Yb₄O(OH)₉NO₃ (phase **4**). Single crystal structures are given for phases **2** and **3** and a full kinetic analysis is carried out.

3.6 Results and Discussion

Initial studies were carried out according to the hydrothermal route outlined in Chapter 2 for $\text{Ln}_2(\text{OH})_5\text{NO}_3 \cdot 1.5\text{H}_2\text{O}$, starting from $\text{Yb}(\text{NO}_3)_3 \cdot 5\text{H}_2\text{O}$, NaOH and NaNO_3 . Reactions were carried out between 100 – 220 °C and metal concentration was varied between 0.20 – 0.50 M. The resulting solid was filtered, washed and allowed to dry in air. The most significant observations are described here, where upon varying the reaction temperature new phases were observed, isolated and characterised. A full kinetic analysis was subsequently carried out and the results will be discussed later on in this chapter.

For clarity, the phases observed are defined as follows;

Phase 1: $\text{Yb}_2(\text{OH})_5\text{NO}_3 \cdot 1.5\text{H}_2\text{O}$, $d = 9.2 \text{ \AA}$.

Phase 2: $\text{Yb}_2(\text{OH})_5\text{NO}_3 \cdot 2\text{H}_2\text{O}$, $d = 9.4 \text{ \AA}$.

Phase 3: $\text{Yb}_2(\text{OH})_5\text{NO}_3 \cdot \text{H}_2\text{O}$, $d = 8.5 \text{ \AA}$.

Phase 4: $\text{Yb}_4\text{O}(\text{OH})_9\text{NO}_3$, $d = 8.0 \text{ \AA}$.

An initial reaction under standard conditions was carried out at 150 °C. The presence of the two phases is apparent in the 3D stack plot of the spectra shown in Figure 9. Bragg reflections corresponding to phase 1 at $d = 9.2 \text{ \AA}$ and phase 2 at $d = 9.4 \text{ \AA}$ are observed, reaching maximum intensity after a period of 50 minutes. The observation of these two phases is consistent with *ex situ* experiments.

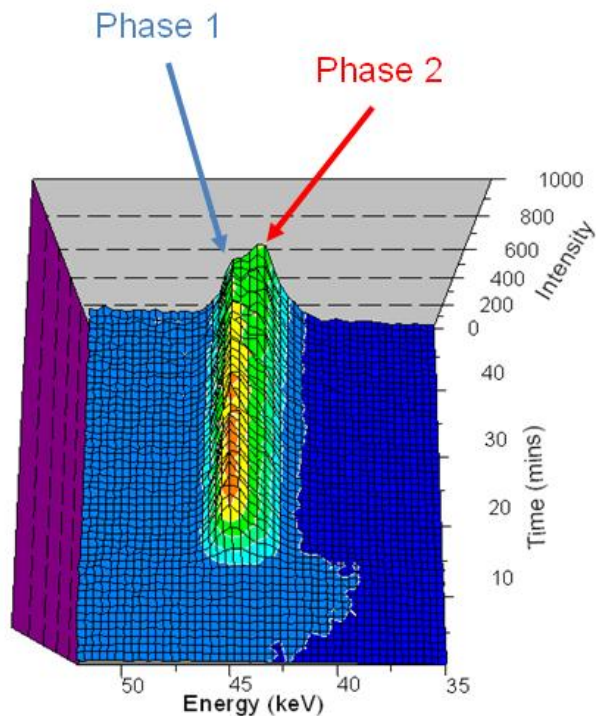


Figure 9 Three-dimensional plot of the evolution of the energy dispersive diffraction pattern with time during the synthesis of $\text{Yb}_2(\text{OH})_5\text{NO}_3 \cdot x\text{H}_2\text{O}$ at 150 °C. The acquisition time for each spectrum was 30 s at a diffraction angle of 1.75 °.

Notably the crystallization of these phases occurs very rapidly, with the phase 1 diffraction peak at $d = 9.2 \text{ \AA}$ appearing after a short induction time of just 15 minutes. Typically the *ex situ* laboratory syntheses of these materials are performed over a period of 48 hours. Undoubtedly these results show that the reactions proceed on a much shorter timescale than this.

At the increased reaction temperature of 175 °C the diffraction peak corresponding to phase 1 at $E = 44.08$ keV ($d = 9.21$ Å) appears after ca. 10 minutes. After a further 10 minutes this peak disappears and is replaced by a Bragg reflection from phase 2 at $E = 43.08$ keV ($d = 9.42$ Å). This reflection quickly reaches maximum intensity and no further change is observed, as Figure 10 shows. The separation of these phases at this temperature facilitated their isolation via an *in situ* quench procedure. This reaction pathway was reproducible making it possible to separate and isolate both the 9.2 Å and 9.4 Å phases by quenching the reaction at an appropriate point.

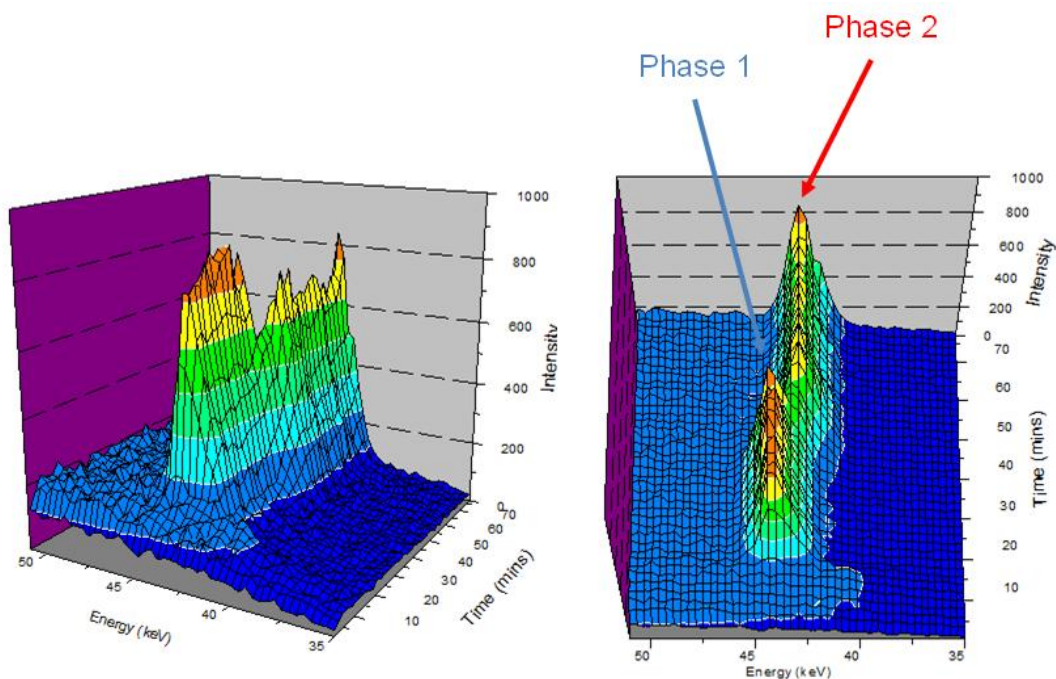


Figure 10 Three-dimensional plots of the evolution of the energy dispersive diffraction pattern with time during the synthesis of $\text{Yb}_2(\text{OH})_5\text{NO}_3 \cdot x\text{H}_2\text{O}$ at 175 °C. The acquisition time for each spectrum was 30 s at a diffraction angle of 1.75 °.

Analysis of the extent of reaction curve shown in Figure 11 reveals more mechanistic information. After an induction period of approximately 400 s both phases **1** and **2** begin to crystallize. After a short period of simultaneous growth the crystallization of **1** becomes dominant and it is not until this phase has passed through its maximum that growth of phase **2** resumes. The intersection of the two curves is at $\alpha \approx 0.5$ implying the loss of coherent diffraction from **1** is matched by the gain in coherence from **2**.

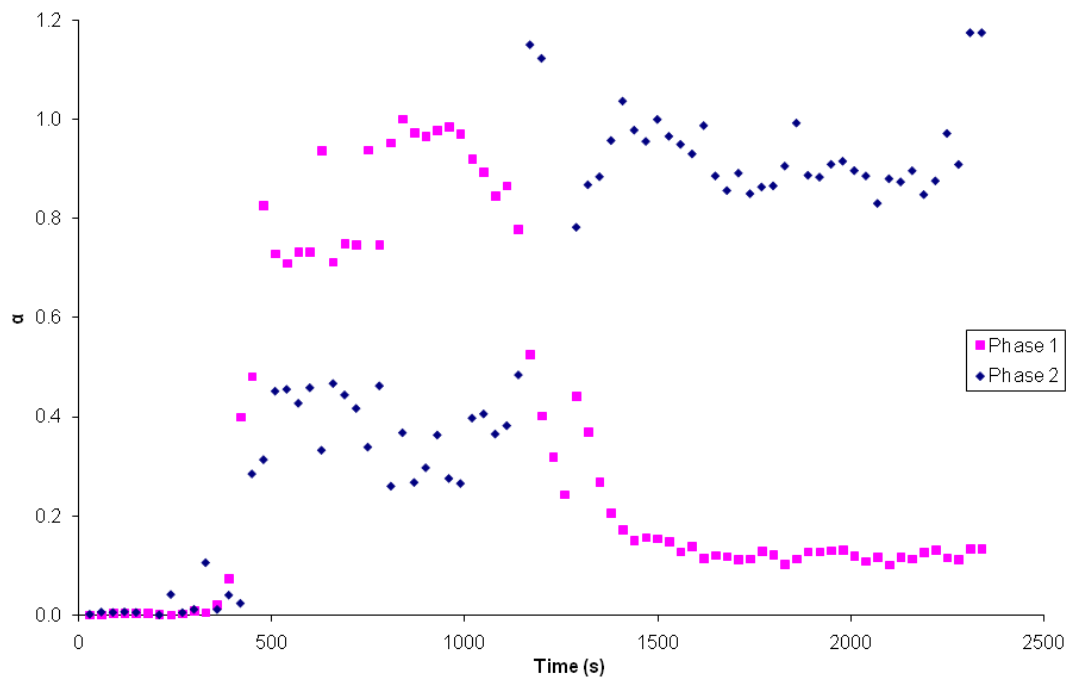


Figure 11 α versus time plot for reaction at 175 °C showing the intersection of phase **1** and phase **2** at $\alpha \sim 0.5$.

It is important to note that phase **2** is particular only to the Yb and Lu materials, experiments under the same conditions for the analogous Y and Er materials yielded only phase **1**. Synthesis under the standard conditions for the Er material was carried out to allow a comparison between metals.

Where *ex situ* synthesis at 150 °C for Yb yields a biphasic mixture, $\text{Er}_2(\text{OH})_5\text{NO}_3 \cdot 1.5\text{H}_2\text{O}$ is produced as a single phase with d-spacing of 9.28 Å. *In situ*, the phase is observed to form after an induction time of 150 seconds, reaching maximum intensity after a period of 1000 seconds with no further transformations observed thereafter, as shown Figure 12.

Sharp-Hancock analysis performed for this data set is shown in Figure 13. Linear regression allows the calculation of exponent of 0.6 which implies that growth is diffusion controlled with deceleratory nucleation in 1 dimension. A rate constant of 0.06 s^{-1} suggests a comparatively fast rate of reaction, when compared to similar reactions of this nature with 10^{-3} s^{-1} reported for ULM-5.⁸

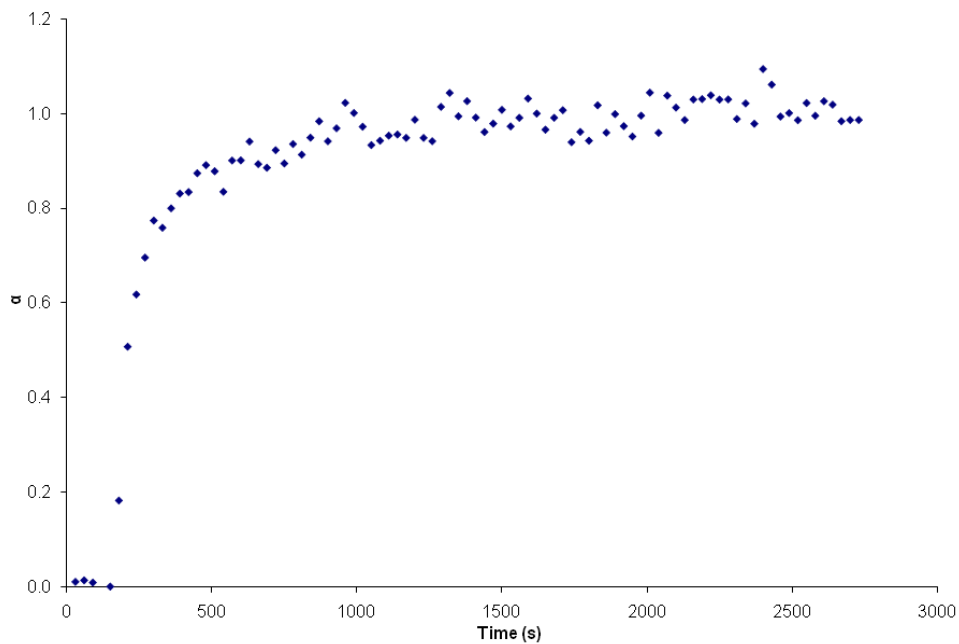


Figure 12 Growth with time of the $d = 9.4 \text{ \AA}$ reflection of $\text{Er}_2(\text{OH})_5\text{NO}_3 \cdot 1.5\text{H}_2\text{O}$ synthesised at $150 \text{ }^\circ\text{C}$.

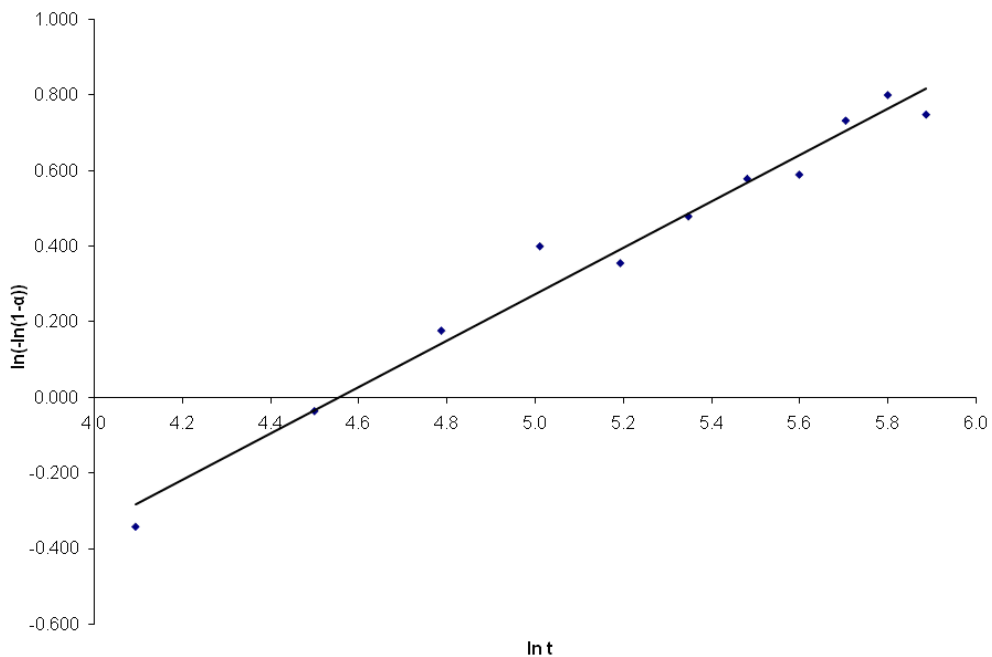


Figure 13 Sharp-Hancock plot of $\ln(-\ln(1-\alpha))$ vs. $\ln t$ for the synthesis of $\text{Er}_2(\text{OH})_5\text{NO}_3 \cdot 1.5\text{H}_2\text{O}$ at $150 \text{ }^\circ\text{C}$.

When the same synthesis is performed at a temperature of 210 °C, significant differences in behaviour are observed. A three-dimensional stack plot of the results is shown in Figure 14. After a short induction period of approximately 5 minutes, the formation of phase **2**, $E = 40.4$ keV ($d = 9.37$ Å) is observed. After 30 minutes this diffraction peak is absent and a diffraction peak from a previously unknown short-lived intermediate, phase **3**, instantly appears at $E = 44.7$ keV ($d = 8.46$ Å). This short-lived phase is present for ca. 10 minutes and was isolated via *in situ* quench procedure in a repeated reaction but was never observed *ex situ* despite extensive screening of reaction conditions. Finally after 40 minutes at this reaction temperature a Bragg reflection at $E = 47.1$ keV ($d = 8.03$ Å) emerges and reaches maximum intensity. After the formation of this phase (**4**), there is no further change in the diffraction pattern. Phase **4** matches a phase formed in the laboratory synthesis after 48 hours at temperatures 175 – 220 °C.

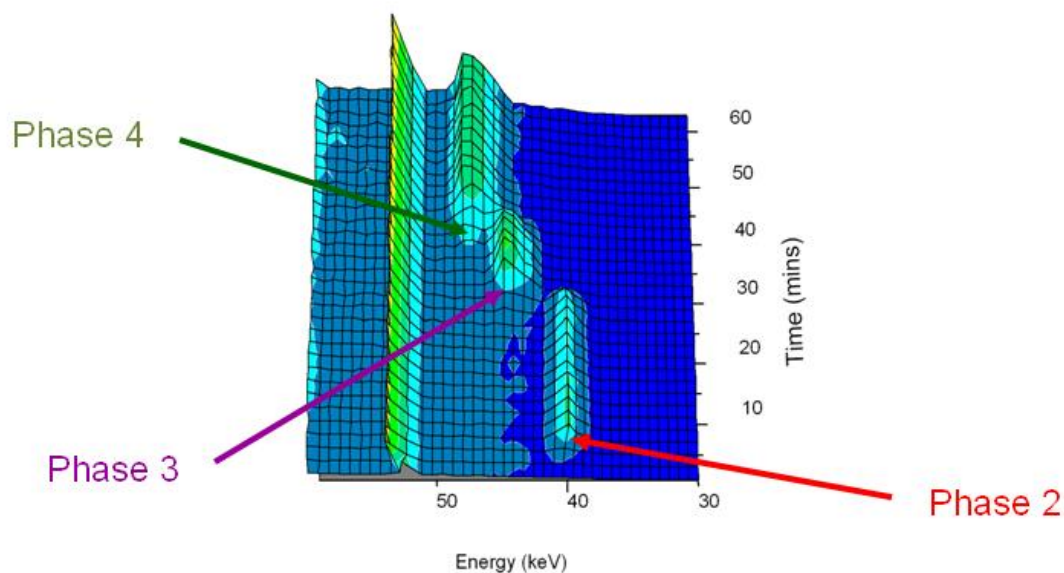


Figure 14 Three-dimensional plot of the evolution of the energy dispersive diffraction pattern with time during the synthesis of $\text{Yb}_2(\text{OH})_5\text{NO}_3 \cdot x\text{H}_2\text{O}$ at 210 °C. The acquisition time for each spectrum was 30 s at a diffraction angle of 1.88 °. Yb cell resonance visible at 51 keV.

The extent of reaction curves for phases 2 – 4 for the reaction at 175 °C are shown in Figure 15. Both the transformation of 2 to 3 and of 3 to 4 intersect at $\alpha \approx 0.4$ suggesting that there is a degree of random nucleation leading to loss of intensity from the first phase before the growth of the second.

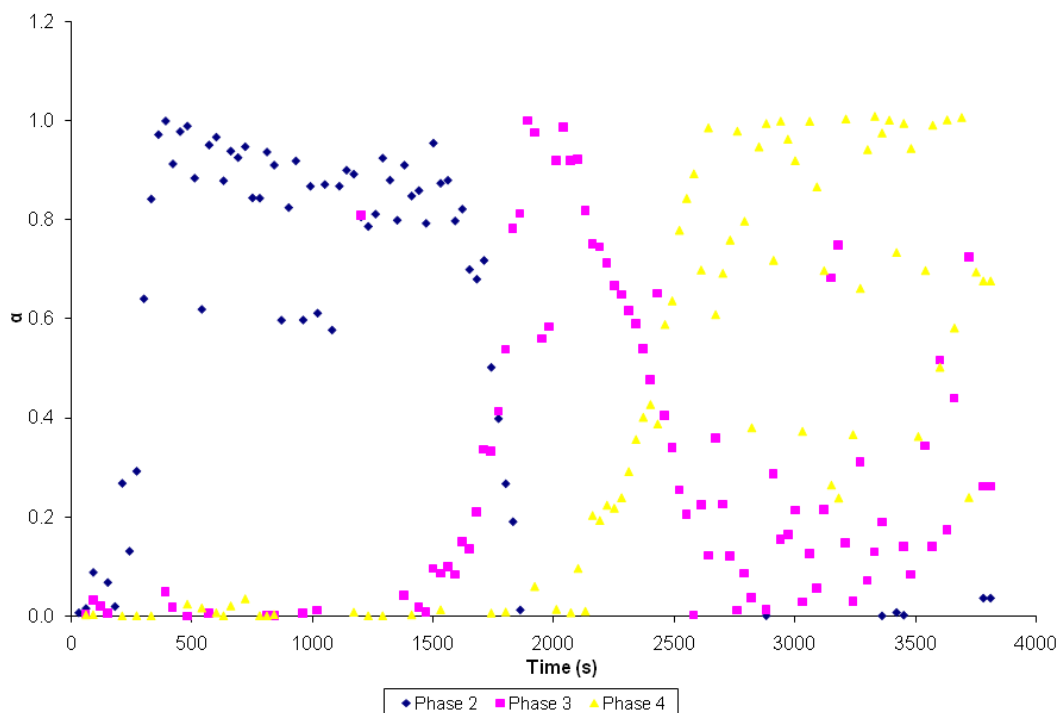


Figure 15 α versus time plot for reaction at 210 °C showing the intersection of phases 2 to 3 and 3 to 4 at $\alpha \sim 0.4$.

3.7 Phase Isolation and Characterisation

3.7.1 Phase 1: $\text{Yb}_2(\text{OH})_5\text{NO}_3 \cdot 1.5\text{H}_2\text{O}$ ($d = 9.2 \text{ \AA}$)

Phase 1 ($\text{Yb}_2(\text{OD})_5\text{NO}_3 \cdot 1.5\text{D}_2\text{O}$) was isolated *in situ* in deuterated form, as it was hoped that neutron diffraction studies would enable elucidation of the structure. The powder X-ray diffraction pattern for phase 1, shown in Figure 16, reveals that this phase has an interlayer separation of 9.22 \AA and is isostructural with the family of hydroxynitrate anion materials discussed in Chapter 2. The low crystallinity of this sample with relatively few non-00 l reflections means that no further structural investigations were possible.

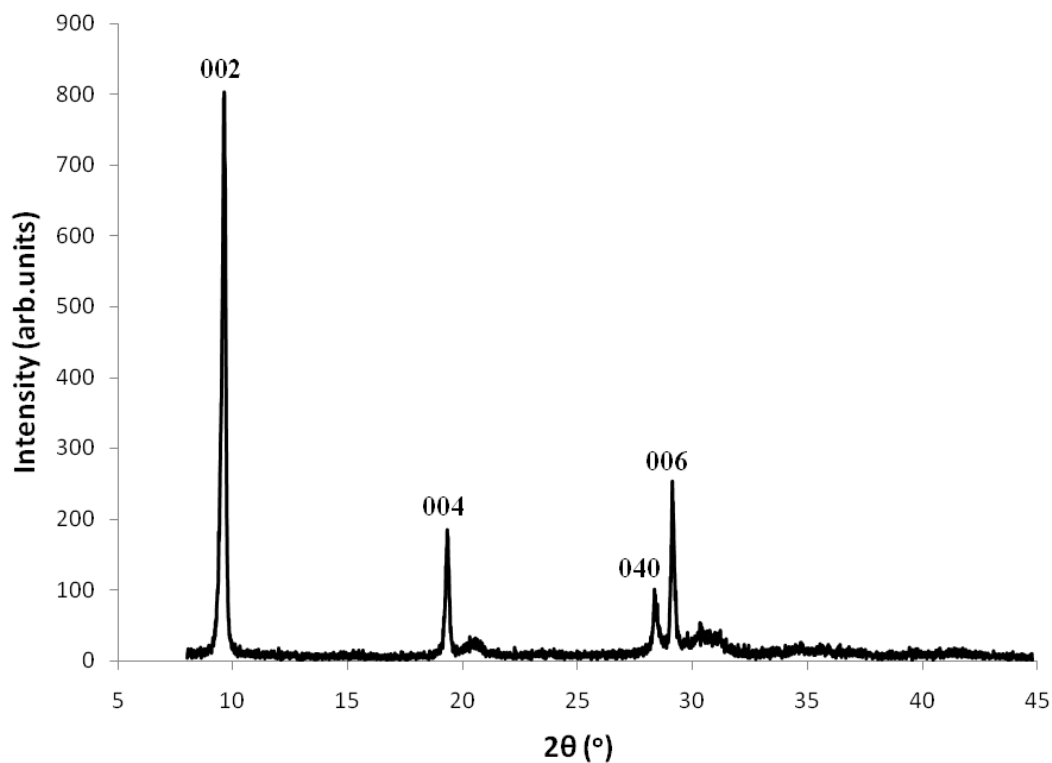


Figure 16 Powder X-ray diffraction pattern for 1.

The TGA data for $\text{Yb}_2(\text{OD})_5\text{NO}_3 \cdot 1.5\text{D}_2\text{O}$ is shown in Figure 17 and displays three distinct mass losses comparable to those seen for other layered hydroxides. The first mass loss of 5.98 % (calculated value is 5.67 %) below 150 °C corresponds to the loss of co-intercalated D_2O . The second mass loss of 7.22 % (8.01 %) by 350 °C corresponds to partial decomposition of the layers leaving a material of nominal composition ' $\text{Yb}_2\text{O}_2(\text{OD})\text{NO}_3$ '.² By 650 °C final decomposition to Yb_2O_3 is complete with a mass loss of 12.12 % (13.92 %). No further mass loss is observed above 650 °C. Deuterium analysis could not be obtained through elemental analysis, however N values are in agreement with calculated values. Calculated N, 2.68 %; found N, 2.70 %.

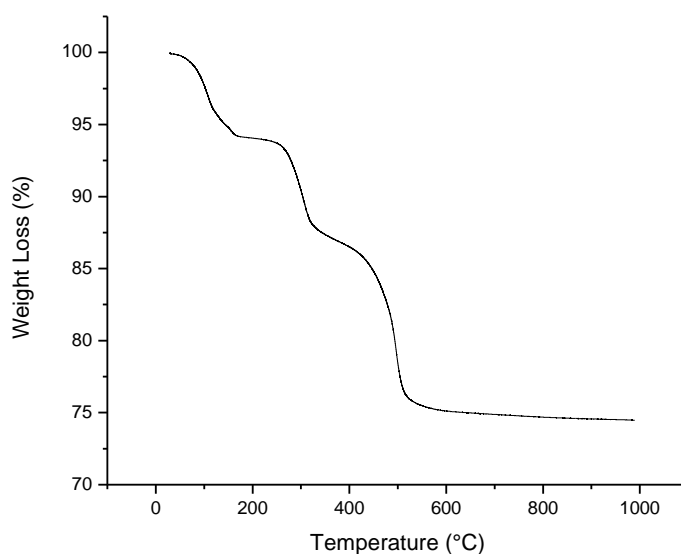


Figure 17 TGA trace for $\text{Yb}_2(\text{OD})_5\text{NO}_3 \cdot 1.5\text{D}_2\text{O}$ (**1**) showing mass losses of 5.98 % below 150 °C and further mass losses of 7.22 % by 350 °C and 12.12 % by 650 °C.

FTIR of **1** (Figure 18) confirms the presence of a nitrate anion by a broad band at approximately 1370 cm^{-1} , other features include a broad absorption band at approximately 3550 cm^{-1} corresponding to a combination of the stretching vibrations of the layer O-D groups and the interlayer D_2O molecules and a bending vibration of D_2O at 1630 cm^{-1} .

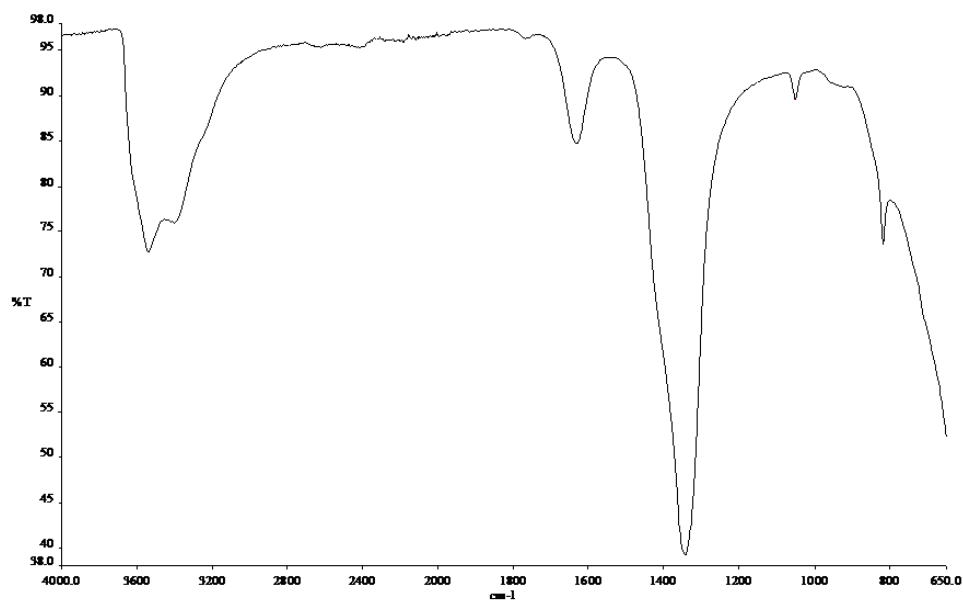


Figure 18 FTIR spectrum of $\text{Yb}_2(\text{OD})_5\text{NO}_3 \cdot 1.5\text{D}_2\text{O}$ (**1**).

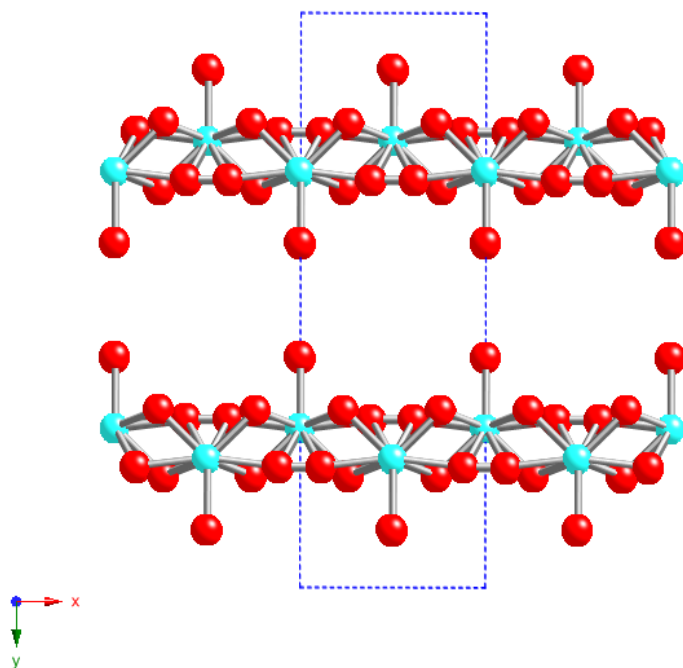
3.7.2 Phase 2: $\text{Yb}_2(\text{OH})_5\text{NO}_3 \cdot 2\text{H}_2\text{O}$ ($d = 9.4 \text{ \AA}$)

Isolation of small single crystals of phase **2** showing d-spacings of 9.39 \AA allowed the partial structure to be elucidated. Structural refinements were carried out by Dr. T. J. Prior following data collection at Station 9.8 at the U.K. SRS, Daresbury Laboratory. The crystal and layer structures are illustrated in Figure 19.

2 crystallises in the centrosymmetric orthorhombic space group *Cmcm* (no. 63) with unit cell parameters $a = 6.0000(12) \text{ \AA}$, $b = 18.589(4) \text{ \AA}$, $c = 3.7555(8) \text{ \AA}$. Details of the structural refinement are contained in Table 3. The asymmetric unit contains a single Yb^{3+} ion and three oxygen atoms, one of which is partially occupied. Hydrogen atoms could not be located in this study; the distinction between bound water and hydroxide is made by reference to the structure. Each hydroxide bridges three Yb ions and this generates layers which are two Yb ions thick. It seems likely on space considerations that nitrate is bound to the layer. The oxygen atom projecting into the interlayer region could correspond to nitrate to give an overall layer $[\text{Yb}_2(\text{OH})_5(\text{NO}_3)]$. The remainder of the nitrate is disordered and not located in this study. There is also evidence for disorder in the position of some of the hydroxide. Each Yb has a formal coordination number of 8.5, indicating the disordered hydroxide leads to variable coordination geometry; one half of the Yb ions are 8-coordinate, while the remainder are 9-coordinate. No interlayer species were identified from the diffraction data.

The unit cell contains two flat $\text{Yb}_2(\text{OH})_5(\text{H}_2\text{O})$ layers extending in the xz plane related by an inversion centre. The result is layers stacked in ABAB fashion along the crystallographic b -axis with an interlayer separation of $9.295(4) \text{ \AA}$. Analysis of the structure by use of the program PLATON³¹ reveals each unit cell contains two voids each of approximately 68 \AA^3 (a total of 31.6 % of the unit cell volume). The small voids may be suitable to contain water.

(a)



(b)

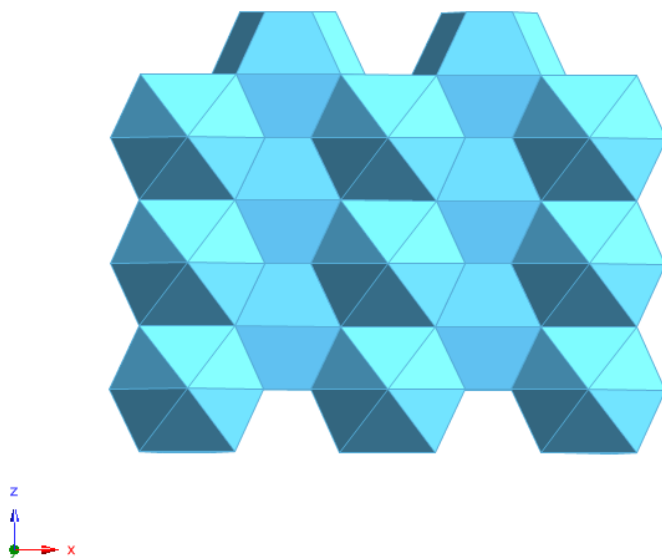


Figure 19 (a) Crystal structure and (b) layer structure of **2** ($d = 9.4 \text{ \AA}$ phase $\text{Yb}_2(\text{OH})_5\text{NO}_3 \cdot 2\text{H}_2\text{O}$).

Table 3 Summary of the crystallographic information for phase 2: $\text{Yb}_2(\text{OH})_5\text{NO}_3 \cdot 2\text{H}_2\text{O}$.

Identification code	lm17c
Empirical formula	O7 Yb2
Formula weight	458.08
Temperature	120(2) K
Wavelength	0.6943 Å
Crystal system	Orthorhombic
Space group	Cmcm
Unit cell dimensions	a / Å
	b / Å
	c / Å
	$\alpha, \beta, \gamma / ^\circ$
Volume	418.87(15) Å ³
Z	2
Density (calculated)	3.632 Mg/m ³
Absorption coefficient	22.168 mm ⁻¹
F(000)	392
Crystal size	0.02 x 0.01 x 0.01 mm ³
Theta range for data collection	3.57 to 31.78°.
Index ranges	$-7 \leq h \leq 8, -23 \leq k \leq 27, -5 \leq l \leq 5$
Reflections collected	1582
Independent reflections	416 [R(int) = 0.0781]
Completeness to theta = 26.00 °	99.6 %
Absorption correction	Semi-empirical from equivalents
Max. and min. transmission	0.801 and 0.668
Refinement method	Full-matrix least-squares on F ²
Data / restraints / parameters	416 / 6 / 21
Goodness-of-fit on F ²	1.095
Final R indices [I > 2sigma(I)]	R1 = 0.0562, wR2 = 0.1395
R indices (all data)	R1 = 0.0901, wR2 = 0.1513
Largest diff. peak and hole	3.195 and -2.952 e.Å ⁻³

The TGA data for **2** (Figure 20) display three distinct mass losses comparable to those seen for **1**, as described in Chapter 2. An initial mass loss of 6.67 % (calculated value for $x = 2$ is 6.78 %) below 150 °C corresponds to the loss of co intercalated water. This is followed by the partial decomposition of the layers, resulting in a mass loss of 6.91 % (7.31 %) by 350 °C leaving a material of nominal composition “Yb₂O₂(OH)NO₃”. Complete decomposition to Yb₂O₃ occurs by 650 °C with a further mass loss of 12.87 % (13.79 %). No further mass loss is observed above 650 °C. Elemental analysis for phase **2** is in agreement with the proposed composition of Yb₂(OH)₅NO₃·2H₂O. Calculated; Yb, 65.40 % N, 2.65 % H, 1.71 %. Observed; Yb, 65.14 % N, 2.86 % H, 1.59 % C, 0.10 %.

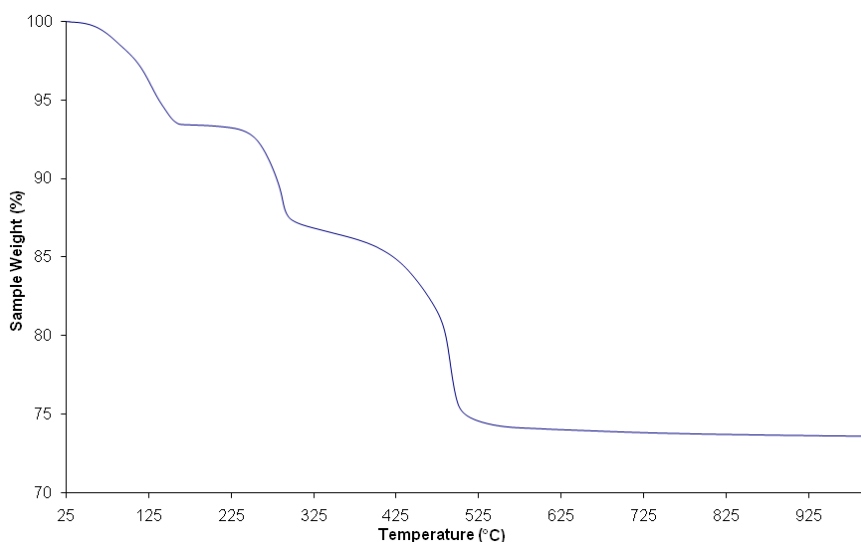


Figure 20 TGA trace for Yb₂(OH)₅NO₃·2H₂O (**2**) showing mass losses of 6.67 % below 150 °C and further mass losses of 6.91 % by 350 °C and 12.87 % by 650 °C.

From the single crystal structure, it seems likely on space considerations that nitrate is bound to the layer. FTIR of **2** (Figure 21) confirms the presence of nitrate by a broad band at approximately 1380 cm^{-1} . However, there is evidence of some splitting in the band at 1380 cm^{-1} indicating coordination of the nitrate anion to the Yb^{3+} cation. Other features include a broad absorption band at approximately 3500 cm^{-1} corresponding to a combination of the stretching vibrations of the layer hydroxyl groups and the interlayer water molecules and a bending vibration of water at 1650 cm^{-1} .

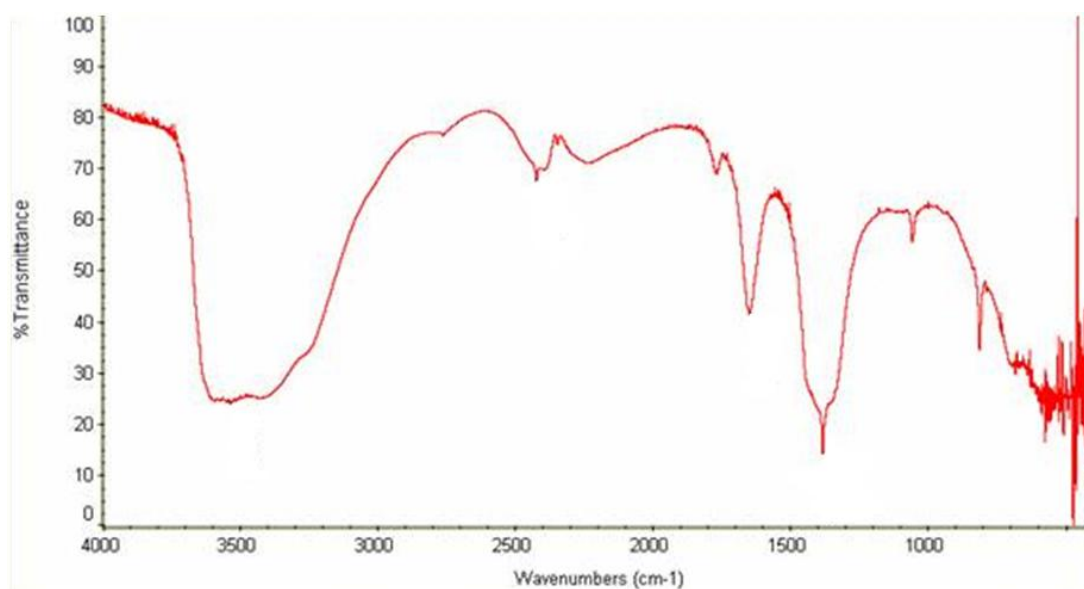


Figure 21 FTIR spectrum of $\text{Yb}_2(\text{OH})_5\text{NO}_3 \cdot 2\text{H}_2\text{O}$ (**2**).

The powder XRD pattern for phase **2** is shown in Figure 22 indicates an interlayer separation of 9.39 \AA . The SEM image of **2** shown in Figure 23 reveals that the material is microcrystalline with rectangular plate morphology.

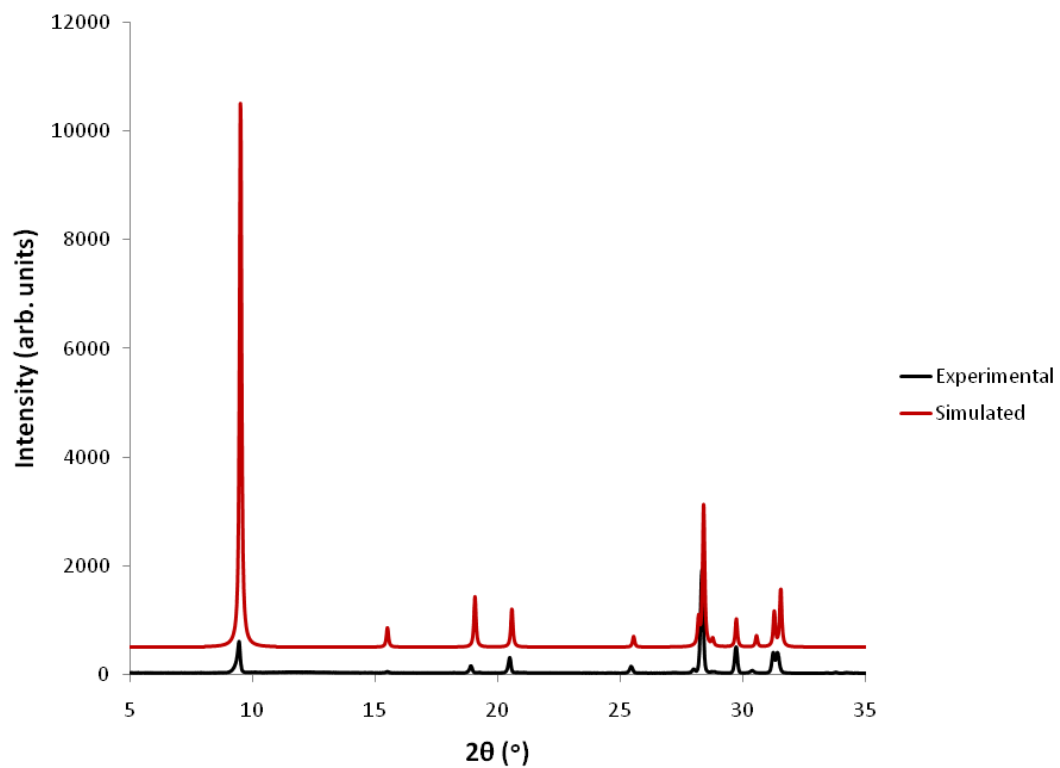


Figure 22 Powder X-ray diffraction pattern for $\text{Yb}_2(\text{OH})_5\text{NO}_3 \cdot 2\text{H}_2\text{O}$ (2).

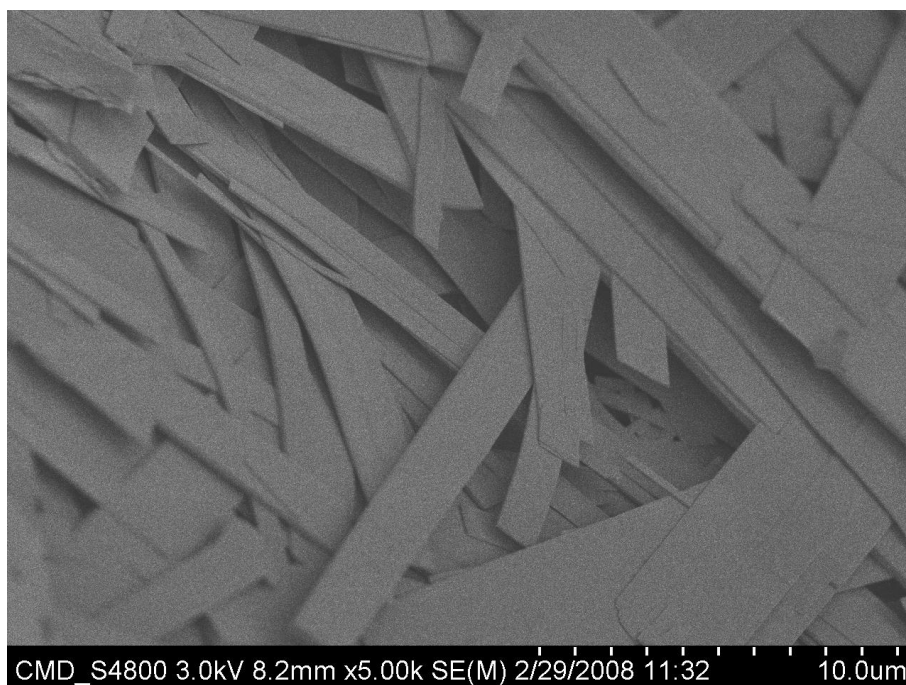


Figure 23 SEM image of $\text{Yb}_2(\text{OH})_5\text{NO}_3 \cdot 2\text{H}_2\text{O}$ (2). (SEM image taken by Mr. G. Evans).

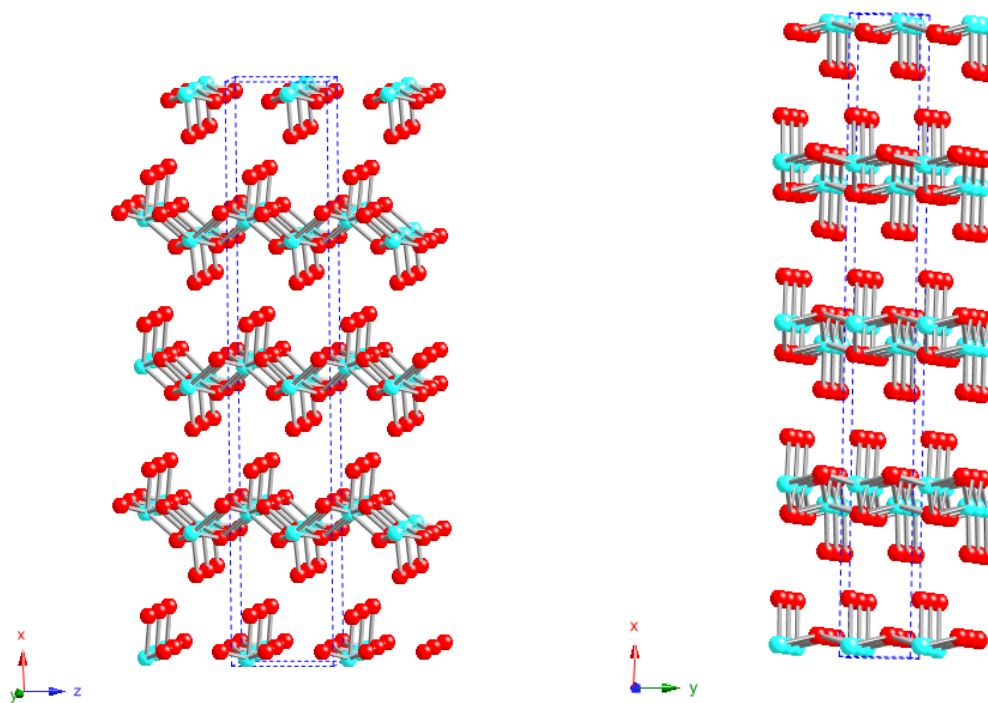
3.7.3 Phase 3: $\text{Yb}_2(\text{OH})_5\text{NO}_3 \cdot \text{H}_2\text{O}$ ($d = 8.5 \text{ \AA}$)

Due to the short-lived nature of the $d = 8.5 \text{ \AA}$ phase, despite extensive screening, it has only been observed and subsequently isolated through *in situ* quenching during EDXRD experiments. As for phase **1**, this phase was isolated in deuterated form ($\text{Yb}_2(\text{OD})_5\text{NO}_3 \cdot \text{D}_2\text{O}$) as it was hoped that neutron diffraction studies would aid elucidation of the structure.

The existence of a layered phase with basal spacing of 8.5 \AA has been reported by Haschke, with lattice parameters of $a = 6.040(4) \text{ \AA}$, $b = 3.800(1) \text{ \AA}$, $c = 8.533(3) \text{ \AA}$ and $a = 5.964(2) \text{ \AA}$, $b = 3.750(1) \text{ \AA}$, $c = 8.526(3) \text{ \AA}$ for $\text{Y}_2(\text{OH})_5\text{NO}_3 \cdot 2\text{H}_2\text{O}$ and $\text{Yb}_2(\text{OH})_5\text{NO}_3 \cdot 2\text{H}_2\text{O}$ respectively.¹ However full crystallographic data, including atom positions were not reported.

Single crystals of $\text{Yb}_2(\text{OH})_5\text{NO}_3 \cdot \text{H}_2\text{O}$ (**3**) were obtained and the crystal and layer structures are illustrated in Figure 24 with full crystallographic details given in Table 4. Structural refinements were carried out by Dr. T. J. Prior on data collected at Station 9.8 at the U.K. SRS, Daresbury Laboratory.

(a)



(b)

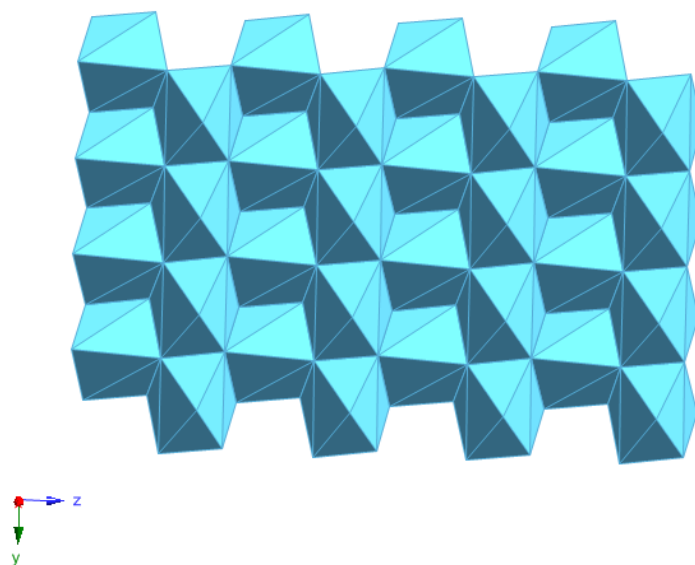


Figure 24 (a) Crystal structure and (b) layer structure of $d = 8.5 \text{ \AA}$ phase $\text{Yb}_2(\text{OH})_5\text{NO}_3 \cdot \text{H}_2\text{O}$ (**3**).

Table 4 Summary of the crystallographic information for phase **3**: $\text{Yb}_2(\text{OH})_5\text{NO}_3 \cdot \text{H}_2\text{O}$.

Identification code	lm8_5_no33
Empirical formula	O3 Yb
Formula weight	221.04
Temperature	120(2) K
Wavelength	0.69430 Å
Crystal system	Orthorhombic
Space group	P n a 21
Unit cell dimensions	a / Å
	b / Å
	c / Å
	$\alpha, \beta, \gamma / ^\circ$
Volume	750.7(2) Å ³
Z	8
Density (calculated)	3.912 Mg/m ³
Absorption coefficient	24.722 mm ⁻¹
F(000)	752
Crystal size	0.035 x 0.01 x 0.005 mm ³
Theta range for data collection	3.53 to 30.91°.
Index ranges	-49 ≤ h ≤ 48, -5 ≤ k ≤ 5, -8 ≤ l ≤ 8
Reflections collected	6912
Independent reflections	1319 [R(int) = 0.0769]
Completeness to theta = 26.00 °	99.2 %
Absorption correction	Semi-empirical from equivalents
Max. and min. transmission	0.7901 and 0.4380
Refinement method	Full-matrix least-squares on F ²
Data / restraints / parameters	1319 / 1 / 35
Goodness-of-fit on F ²	1.139
Final R indices [I > 2σ(I)]	R1 = 0.0846, wR2 = 0.2486
R indices (all data)	R1 = 0.0959, wR2 = 0.2585
Absolute structure parameter	0.1(3)
Largest diff. peak and hole	11.088 and -9.101 e.Å ⁻³

3 crystallises in the non-centrosymmetric space group $Pna2_1$ (no. 33) with unit cell parameters $a = 33.866(5) \text{ \AA}$, $b = 3.3705(6) \text{ \AA}$, $c = 5.9417(10) \text{ \AA}$. A summary of crystallographic data is contained in Table 4. The asymmetric unit contains two independent Yb^{3+} ions, each of which is bound by three oxygen atoms. Yb1 and O1, O2, O3 form a single layer, while coordination of Yb2 by O4, O5, and O6 produces a second independent layer. O1, O2, O4, and O5 are likely to be hydroxide: each one bridges between three Yb cations. The remaining oxygen atoms project perpendicular to these layers suggesting these may be hydroxide or nitrate. Hydrogen atoms were not located in this study. Assuming a 50:50 distribution of hydroxide and nitrate in these sites, the layer composition would be $[\text{Yb}_2(\text{OH})_5(\text{NO}_3)]$. Additional water molecules present between the layers were not located crystallographically.

Within each layer the Yb is 7-coordinate: both Yb1 and Yb2 adopt distorted capped trigonal prismatic geometry. In each case the capping atom (hydroxide or nitrate) projects into the interlayer region. Each unit cell contains four layers, stacked along the crystallographic a -axis at a distance of $8.467(5) \text{ \AA}$. The layers lie in an approximate AAAA orientation, although they do not directly overlie. The structure is pseudocentrosymmetric and close to adopting the space group $Pnma$. However, introducing a centre of symmetry does not allow for distortion of the Yb polyhedra. Each unit cell contains a void space of about 90 \AA^3 within which unbound water may be located.

The TGA data for **3** (Figure 25) show three mass losses, an initial mass loss of 3.09 % (calculated value for $x = 1$ is 3.52 %) below $150 \text{ }^\circ\text{C}$ corresponding to the loss of co intercalated water. A second mass loss indicates the partial decomposition of the layers, resulting in a mass loss of 8.96 % (7.31 %) by $350 \text{ }^\circ\text{C}$ leaving a material of nominal composition “ $\text{Yb}_2\text{O}_2(\text{OH})\text{NO}_3$ ”. A further mass loss of 12.75 % (13.79 %) yielding Yb_2O_3 occurs by $650 \text{ }^\circ\text{C}$ with no further mass loss observed above $650 \text{ }^\circ\text{C}$. Elemental analysis for phase **3** is consistent with this composition; calculated: N, 2.69 %, observed: N, 2.90 %.

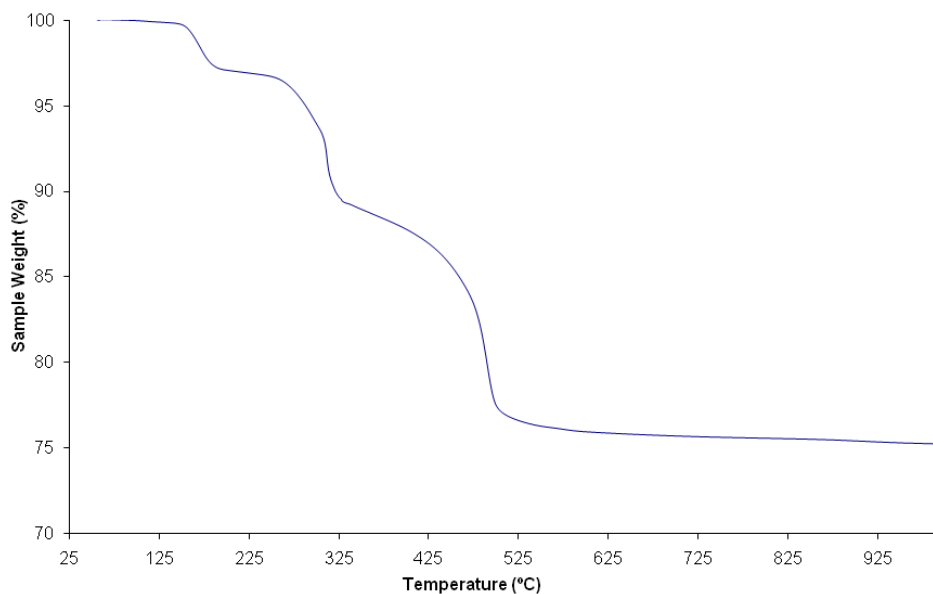


Figure 25 TGA for $\text{Yb}_2(\text{OH})_5\text{NO}_3 \cdot \text{H}_2\text{O}$ (**3**) showing mass losses of 3.09 % below 150 °C and further mass losses of 8.96 % by 350 °C and 12.75 % by 650 °C.

FTIR of **3** is shown in Figure 26 with a broad absorption at approximately 3500 cm^{-1} corresponding to a combination of the stretching vibrations of the layer hydroxyl groups and the interlayer water molecules and a bending vibration of water at 1630 cm^{-1} . A broad absorption band at 1380 cm^{-1} confirms the presence of a nitrate anion. Increased splitting in the region $1300 - 1450 \text{ cm}^{-1}$ suggests that the nitrate in this material is more strongly bound than in phase **2**.

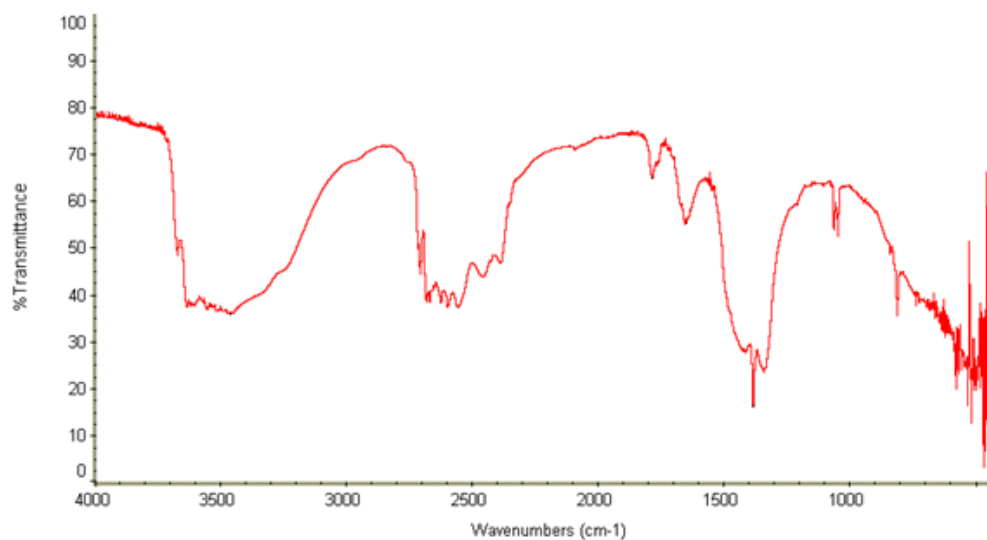


Figure 26 FTIR spectrum of $\text{Yb}_2(\text{OH})_5\text{NO}_3 \cdot \text{H}_2\text{O}$ (**3**).

A comparison of the FTIR spectra for phases **1**, **2** and **3** with those reported by Newman and Jones in a previous study of hydroxynitrates allows the coordination environment of NO_3^- to be investigated further. The materials $\text{Zn}_5(\text{OH})_8(\text{NO}_3)\cdot 2\text{H}_2\text{O}$, $\text{Cu}_2(\text{OH})_3\text{NO}_3$, $\text{Ni}_2(\text{OH})_3\text{NO}_3$ and $\text{La}(\text{OH})_2\text{NO}_3$ were studied and their FTIR data are illustrated in Figure 27.

In $\text{Zn}_5(\text{OH})_8(\text{NO}_3)\cdot 2\text{H}_2\text{O}$ the interlayer nitrate is uncoordinated and results in a single absorption band at 1370 cm^{-1} . Whilst for $\text{La}(\text{OH})_2\text{NO}_3$ in which the nitrate anion is strongly bonded to La, absorption bands occur in the region $1300 - 1450\text{ cm}^{-1}$.

The nitrate species in both $\text{Cu}_2(\text{OH})_3\text{NO}_3$ and $\text{Ni}_2(\text{OH})_3\text{NO}_3$ is less strongly coordinated to the metal cation than in the La material. This coordination in the case of $\text{Cu}_2(\text{OH})_3\text{NO}_3$ gives rise to bands at 1428 and 1341 cm^{-1} (asymmetric and symmetric NO_2 stretches) with a further band observed at 1047 cm^{-1} due to an N-O stretch. For $\text{Ni}_2(\text{OH})_3\text{NO}_3$ splitting in the region $1300 - 1450\text{ cm}^{-1}$ is increased and the N-O stretch frequency reduced. These observations support the assertion that the nitrate anion in the Ni material is bound more strongly to the hydroxide layer than in the Cu material.

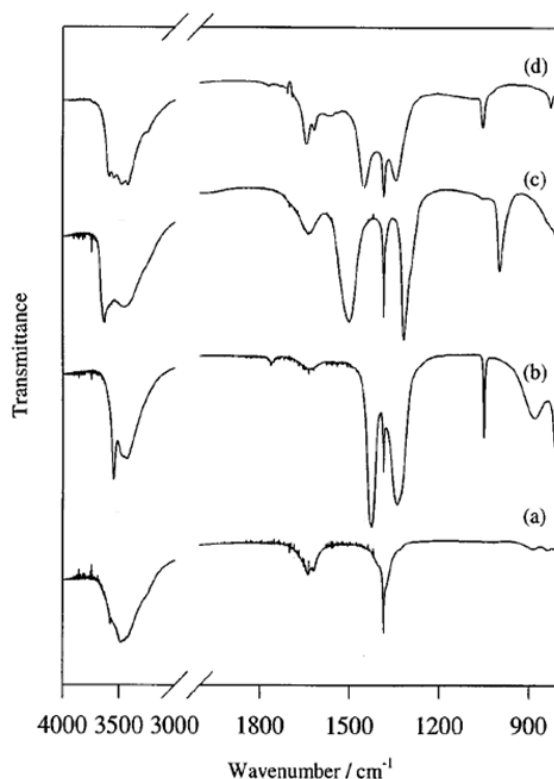


Figure 27 FTIR spectra of (a) $\text{Zn}_5(\text{OH})_8(\text{NO}_3)\cdot 2\text{H}_2\text{O}$, (b) $\text{Cu}_2(\text{OH})_3\text{NO}_3$, (c) $\text{Ni}_2(\text{OH})_3\text{NO}_3$ and (d) $\text{La}(\text{OH})_2\text{NO}_3$.³²

By comparing the FTIR spectra of phases **1**, **2** and **3** directly, as shown in Figure 28, the coordination environment of NO_3^- in the $\text{Yb}_2(\text{OH})_5\text{NO}_3 \cdot x\text{H}_2\text{O}$ materials can be investigated further. Firstly in the case of Phase **1** ($\text{Yb}_2(\text{OH})_5\text{NO}_3 \cdot 1.5\text{H}_2\text{O}$) the presence of uncoordinated nitrate between the layers is evidenced by the single absorption at 1370 cm^{-1} . In phase **2** there is evidence of splitting in the band at 1380 cm^{-1} indicating coordination of the nitrate anion to the Yb^{3+} cation. In phase **3**, splitting in the region $1300 - 1450 \text{ cm}^{-1}$ is increased indicating that the nitrate in this material is more strongly bound than in phase **2**.

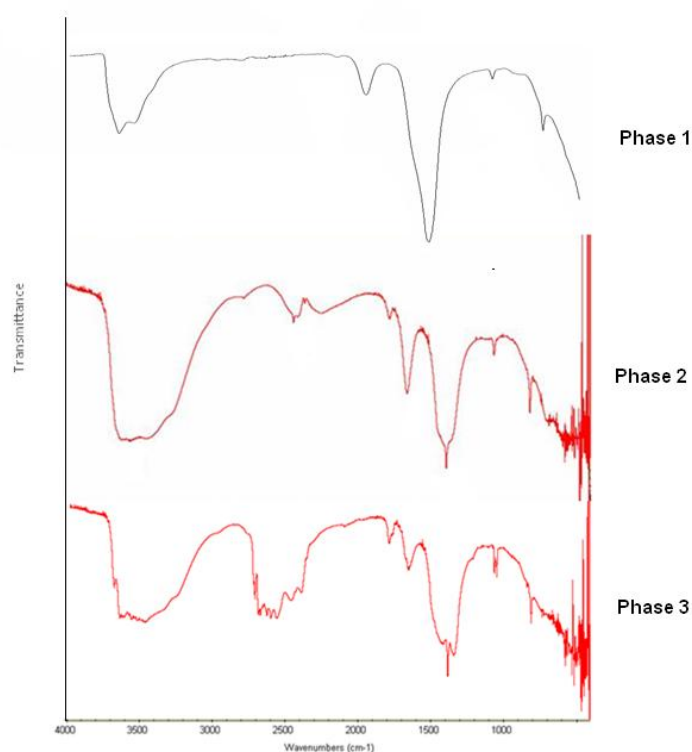


Figure 28 FTIR spectra of phases **1**, **2** and **3**.

A powder XRD pattern for the *in situ* quenched phase **3** is shown in Figure 29. The pattern is typical of a layered phase and displays a d-spacing of 8.54 \AA . There is also a small amount of $d = 9.2 \text{ \AA}$ (phase **1**) present as an impurity. This is perhaps surprising, given that during the *in situ* experiment at $175 \text{ }^\circ\text{C}$ phase **1** is not observed (Figure 14). As this material was isolated via *in situ* quenching, it is most likely that the presence of a small amount of this phase results from residual amounts of phase **2**, $d = 9.4 \text{ \AA}$ in the sample which has collapsed upon drying to give $d = 9.2 \text{ \AA}$.

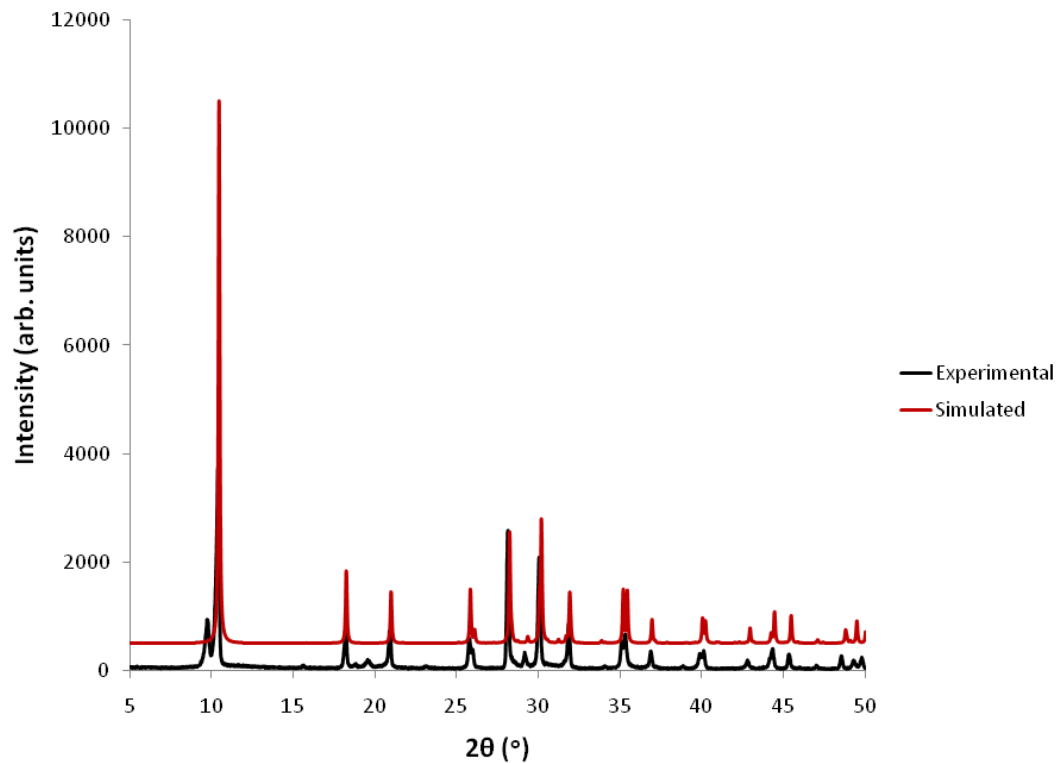


Figure 29 Powder X-ray diffraction pattern for $\text{Yb}_2(\text{OH})_5\text{NO}_3 \cdot \text{H}_2\text{O}$ (**3**).

SEM reveals that **3** is of intermediate morphology between materials **2** and **4**, with distorted rectangular plates as well as some small needle crystallites, as shown in Figure 30.

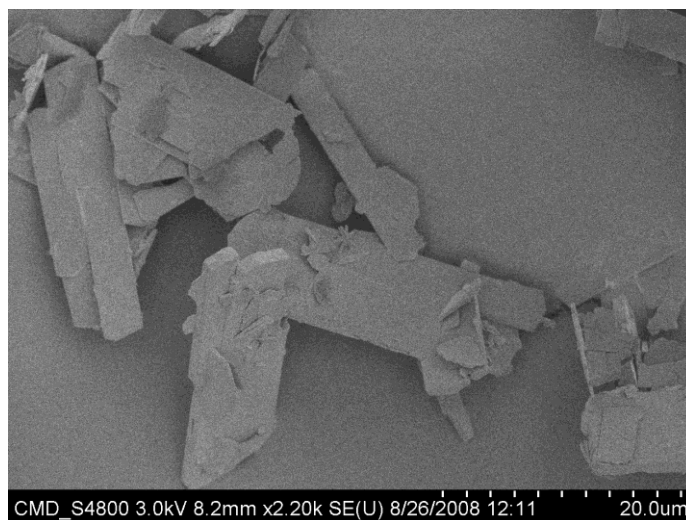


Figure 30 SEM image of $\text{Yb}_2(\text{OH})_5\text{NO}_3 \cdot \text{H}_2\text{O}$ (**3**). (Mr G. Evans).

3.7.4 Phase 4: $\text{Yb}_4\text{O}(\text{OH})_9\text{NO}_3$

The intermediate phase 8.5 Å phase undergoes a final transformation to $\text{Yb}_4\text{O}(\text{OH})_9\text{NO}_3$ (4), a 3D framework structure with 1D channels containing uncoordinated NO_3^- ions, shown in Figure 31. The material is isostructural with $\text{Y}_4\text{O}(\text{OH})_9\text{NO}_3$ ³³ and $\text{Er}_4\text{O}_2(\text{OH})_8\cdot\text{HNO}_3$,³⁴ although it is likely that the proton distribution in the Er compound is incorrect. $\text{Yb}_4\text{O}(\text{OH})_9\text{NO}_3$ adopts a monoclinic structure with space group $\text{P}2_1$. Unit cell parameters obtained by a Rietveld refinement (Figure 32) are $a = 9.28415(14)$ Å, $b = 16.24241(21)$ Å, $c = 3.55823(7)$ Å, $\beta = 101.1378(35)$ °. The unit cell contains two formula units of $\text{Yb}_4\text{O}(\text{OH})_9\text{NO}_3$ and 8 Yb atoms, two of which are 9-coordinate to hydroxyl groups. The six remaining Yb atoms are 7-coordinate with each coordinated to two O^{2-} and five hydroxyls. The nitrate anions in the channels randomly assume two 50 % occupancy orientations in the channels. The crystallographic details of the refinement are given in Table 5 and refined atomic coordinates in Table 6. In the refinement it was not possible to fully refine the oxygen positions and as a result, soft constraints were applied throughout. This was especially necessary for the oxide which possibly suggests a degree of disorder in its position. The nitrate position was not refined and assumed to be as in the reported Y and Er materials.

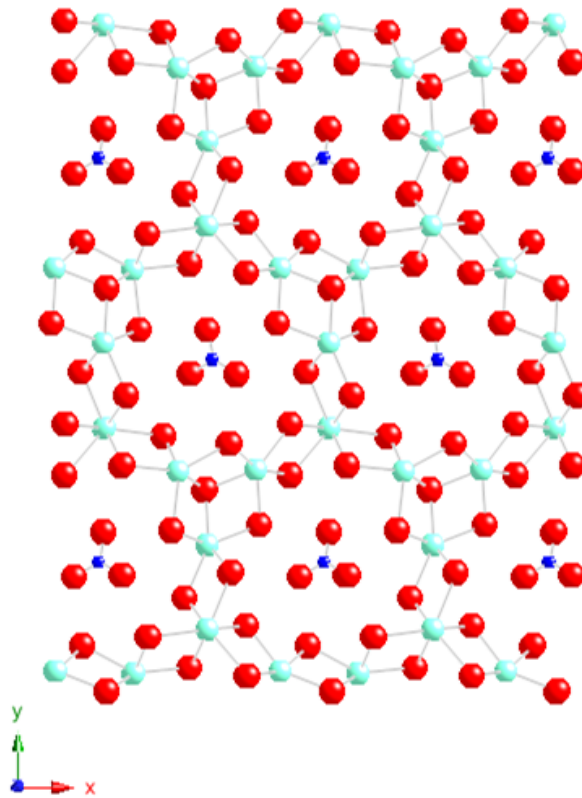


Figure 31 Crystal structure of $d = 8.0 \text{ \AA}$ phase $\text{Yb}_4\text{O}(\text{OH})_9\text{NO}_3$ (4).

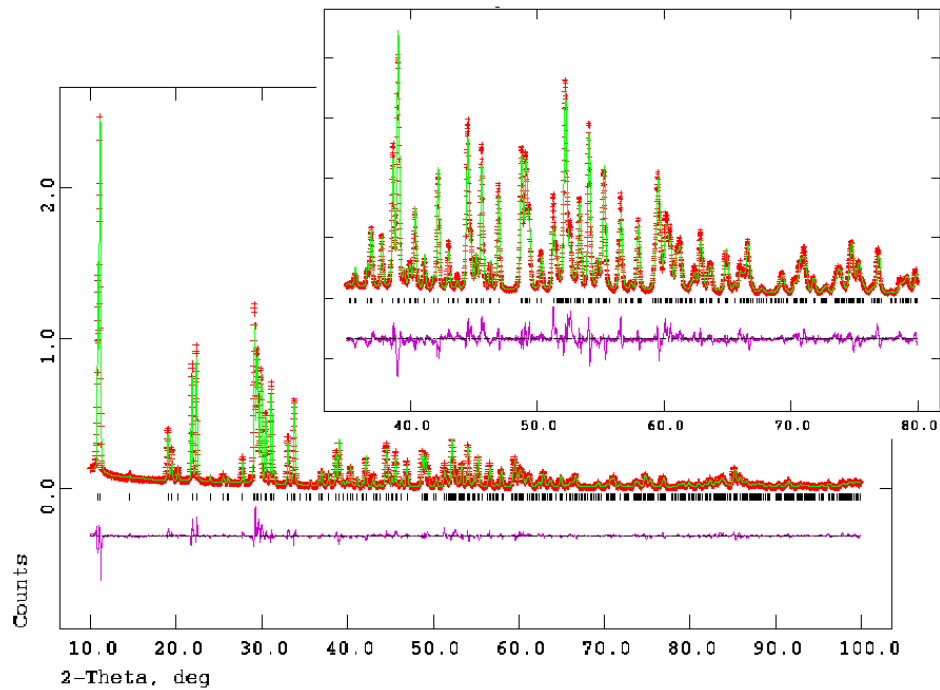


Figure 32 Rietveld refinement for phase 4.

Table 5 Summary of the crystallographic data for $\text{Yb}_4\text{O}(\text{OH})_9\text{NO}_3$.

	$\text{Yb}_4\text{O}(\text{OH})_9\text{NO}_3$
a (Å)	9.28415(14)
b (Å)	16.24241(21)
c (Å)	3.55823(7)
α, β, γ (°)	90, 101.1378(35), 90
Volume (Å ³)	526.463(10)
Cell	Monoclinic
Spacegroup	$P2_1$
No. parameters refined	60
Radiation type, λ	X-ray, 1.54051 Å
No. reflections	576
Preferred orientation	1.29(1)
R_p	9.01
wR_p	11.57
R_f^2	7.319
χ^2	10.36

Table 6 Fractional atomic coordinates for $\text{Yb}_4\text{O}(\text{OH})_9\text{NO}_3$.

Atom	x	y	z
Yb1	0.2669(4)	0.0026(10)	0.6397(31)
Yb2	0.7290(4)	0.2910(10)	0.8826(35)
Yb3	0.05459(26)	0.1882(10)	0.5145(26)
Yb4	0.40100(26)	0.1850(10)	0.1729(29)
O1	0.0001(27)	0.0417(15)	0.351(12)
O2	0.2797(22)	0.1359(14)	0.613(8)
O3	0.1726(20)	0.2683(15)	0.079(8)
O4	0.4615(26)	0.0333(15)	0.254(15)
O5	0.6535(19)	0.1949(16)	0.352(8)
O6	0.8979(21)	0.2989(16)	0.471(8)
O7	0.8869(19)	0.1678(18)	0.931(8)
O8	0.4569(21)	0.2763(19)	0.722(10)
O9	0.8549(24)	0.4289(14)	0.722(10)
O10	0.6348(23)	0.3686(15)	0.331(8)
O11	0.147	0.414	0.035
O12	0.273	0.534	0.061
O13	0.348	0.437	0.418
O14	0.20816	0.43914	0.8545
N1	0.262	0.458	0.149

The TGA data for **4**, shown in Figure 33 display two distinct mass losses. An initial mass loss of 7.84 % below 350 °C corresponds to the hydroxide groups with the loss of four molecules of water (calculated mass loss = 7.81 %). Complete decomposition to Yb_2O_3 occurs by 650 °C with a further mass loss of 6.77 % (6.82 %). Elemental analysis for phase **4** is in agreement with the proposed composition of $\text{Yb}_4\text{O}(\text{OH})_9\text{NO}_3$. Calculated; Yb, 74.97 % N, 1.52 % N, 0.98 %. Observed; Yb, 74.55 % N, 1.43 % H, 0.91 % C, 0.16 %.

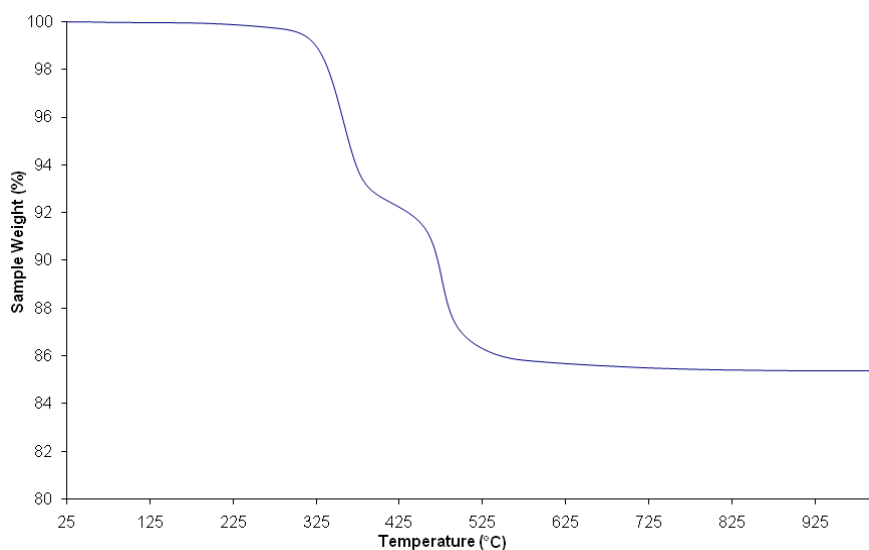


Figure 33 TGA trace for $\text{Yb}_4\text{O}(\text{OH})_9\text{NO}_3$ (**4**) showing mass losses of 7.84 % below 350 °C and a further mass loss of 6.77 % by 650 °C.

FTIR for **4** (Figure 34) confirms the presence of an uncoordinated nitrate anion by a broad band at approximately 1370 cm^{-1} , with a broad absorption band at approximately 3500 cm^{-1} corresponding to stretching vibrations of the layer hydroxyl groups.

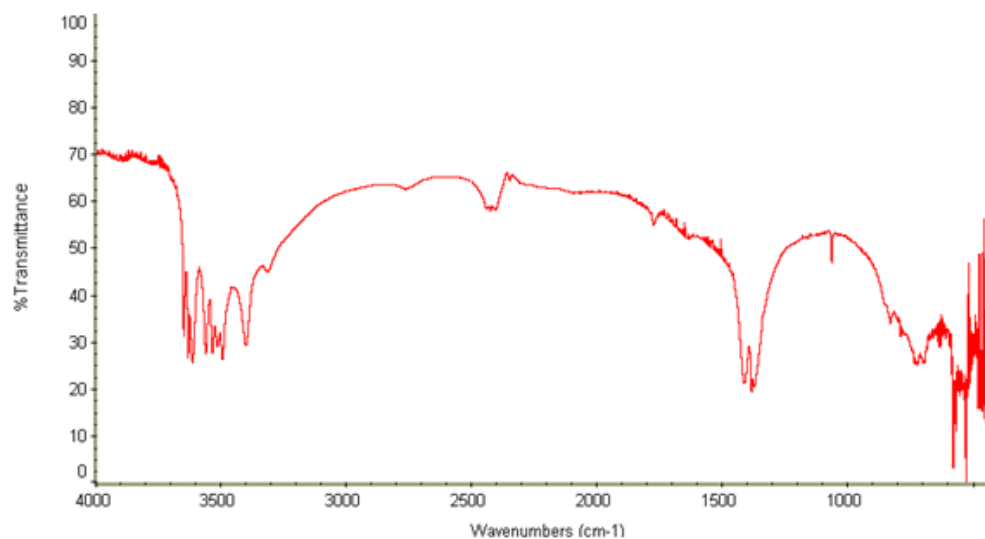


Figure 34 FTIR spectrum for $\text{Yb}_4\text{O}(\text{OH})_9\text{NO}_3$ (**4**).

SEM imaging (Figure 35) shows that the material is microcrystalline with needle morphology. $\text{Yb}_4\text{O}(\text{OH})_9\text{NO}_3$ can be synthesised directly *ex situ* at temperatures above $175\text{ }^\circ\text{C}$ with reaction times of 48 hours.



Figure 35 SEM image for phase 4, $\text{Yb}_4\text{O}(\text{OH})_9\text{NO}_3$ (Mr. G. Evans).

3.7.5 Anion Exchange

One characteristic property of the layered hydroxides is their ability to undergo anion exchange reactions with a variety of inorganic and organic anions. For the $\text{Ln}_2(\text{OH})_5\text{NO}_3 \cdot 1.5\text{H}_2\text{O}$ ($\text{Ln} = \text{Tb} - \text{Tm}$) phases, which were discussed in Chapter 2 anion exchange was demonstrated with a range of anions and exchange was shown to be facile. Anion exchange reactions were once again employed here to investigate the reactivity of the interlayer region and discover the effects of the differences in layer composition and structure between phases **2** and **3**. Anion exchange for phase **4** with terephthalate proved unsuccessful between room temperature and 60 °C, although this is most likely to be due to anion size with respect to channel size. Exchange with Cl^- however also proved unsuccessful suggesting that the channels are inaccessible.

Room temperature anion exchange reactions with sodium terephthalate for **2** and **3** proved unsuccessful. The appearance of very small Bragg reflections at $d = 13.3 \text{ \AA}$ suggests that a small amount of partial exchange was possible at 60 °C when stirred for 7 days. This indicates that the nitrate anions in the layered species may be directly coordinated to the Yb^{3+} cation, as evidenced by FTIR and is analogous to the previously reported $\text{La}(\text{OH})_2\text{NO}_3 \cdot \text{H}_2\text{O}$ ³², where prolonged heating was required to bring about complete anion exchange with acetate, benzoate and terephthalate. Powder X-ray diffraction data for the anion exchange intercalates is shown for phase **2** in Figure 36 and phase **3** in Figure 37.

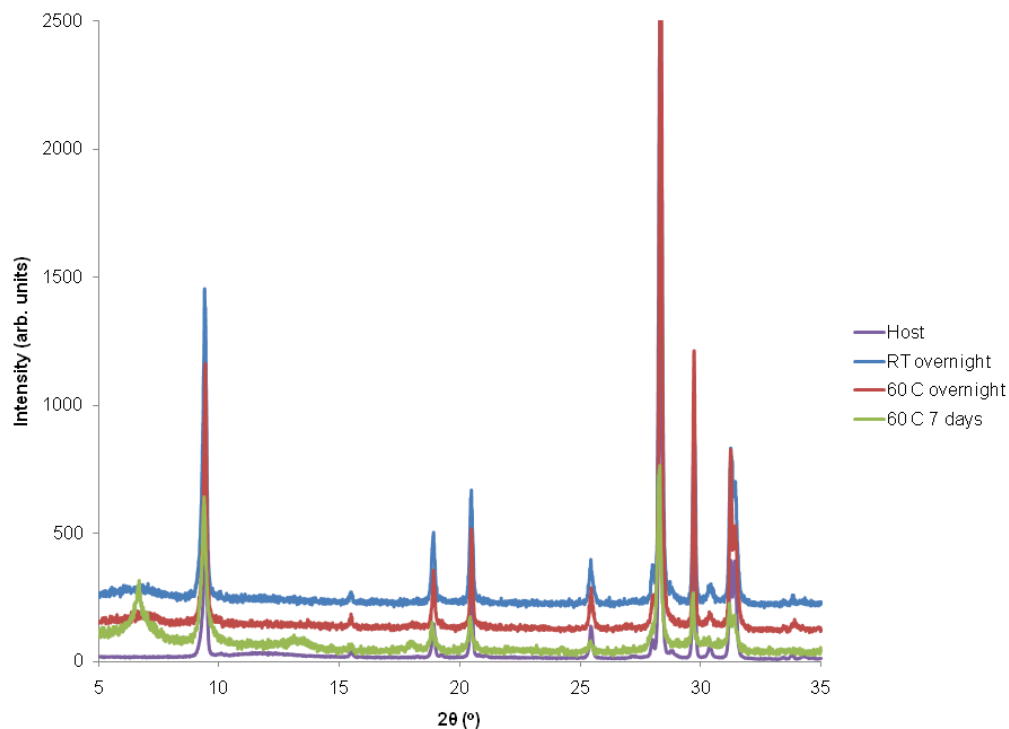


Figure 36 Powder XRD diffraction patterns of the anion exchange reactions of sodium terephthalate with phase **2**; at room temperature overnight, 60 °C overnight and 60 °C for 7 days.

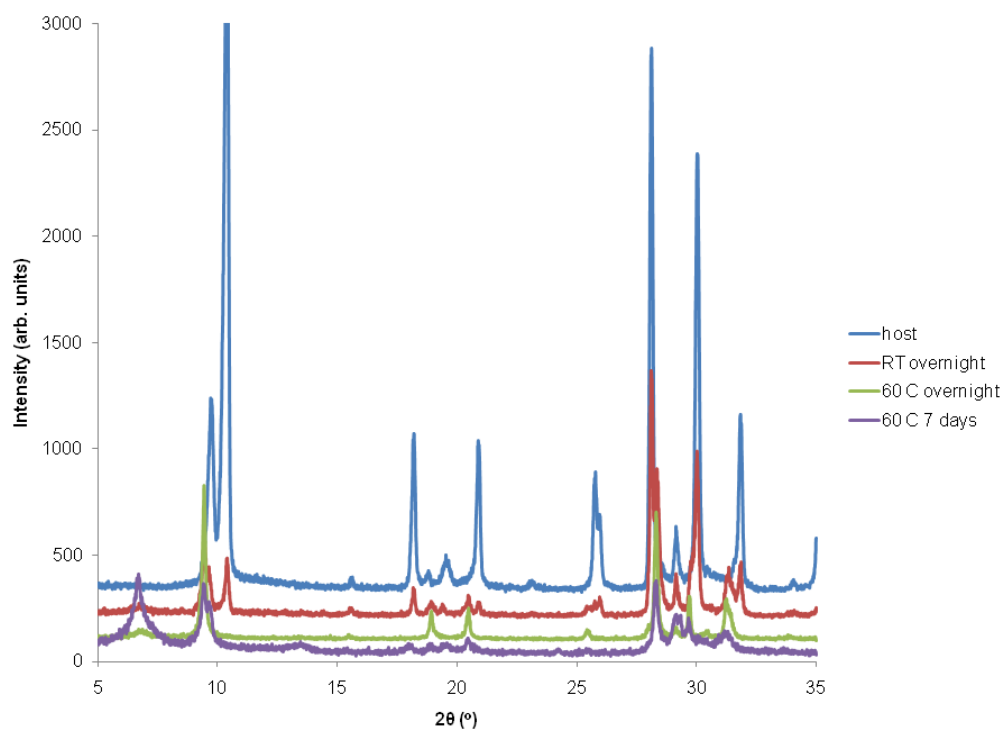


Figure 37 Powder XRD diffraction patterns of the anion exchange reactions of sodium terephthalate with phase **3**; at room temperature overnight, 60 °C overnight and 60 °C for 7 days.

3.8 Kinetic Analysis

Knowledge of solid state reaction kinetics allows both quantitative information to be gathered specifically in terms of rate constants, activation energies and qualitative information allowing reaction mechanisms to be deduced.

3.8.1 Temperature dependency experiments

To ascertain the effects of temperature on the synthesis of phases **1** - **4** reactions were carried out between 100 – 220 °C whilst retaining the standard reaction composition for both *in situ* and *ex situ* reactions. In *ex situ* experiments, biphasic mixtures of phases **1** and **2** were obtained at temperatures 100 – 150 °C and reactions at temperatures exceeding 175 °C afforded phase **4** (Table 7).

Table 7 Phases isolated from *ex situ* temperature dependency experiments.^a

T (°C)	Phase	d – spacing (Å)
100	1 and 2	9.14, 9.34
125	1 and 2	9.19, 9.39
150	1 and 2	9.22, 9.44
175	4	7.98, 8.15
200	4	7.97, 8.14
210	4	7.95, 8.12
220	4	7.97, 8.14

^a *Ex situ* experiments were carried out for a period of 48 hours.

It was decided to monitor the reaction kinetics using EDXRD at 100 °C as it was anticipated that this reaction would be the slowest. Figure 38 shows that crystallisation even at this temperature proceeds very rapidly following an induction period of approximately 600 seconds.

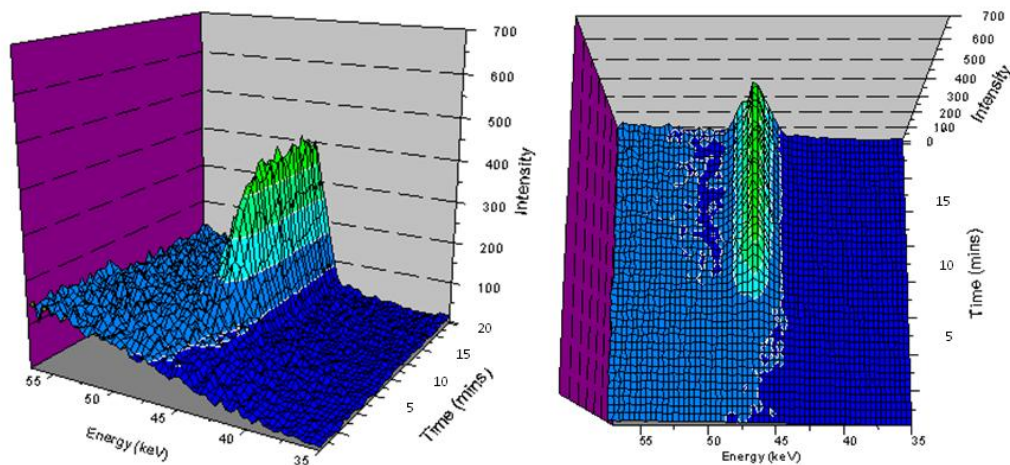


Figure 38 Three-dimensional plot of the evolution of the energy dispersive diffraction pattern with time during the synthesis of $\text{Yb}_2(\text{OH})_5\text{NO}_3 \cdot 1.5\text{H}_2\text{O}$ at 100°C . The acquisition time for each spectrum was 30 s at a diffraction angle of 1.83° .

In the first instance kinetic data can be extracted from the growth curve shown in Figure 39. Notably, this plot of extent of reaction, α against time in seconds shows that after only 400 seconds a weak Bragg reflection corresponding to the initial nucleation of phase **2** begins to appear. However, this initial formation of phase **2** appears to be followed by a period of equilibration as α then remains constant after 500 seconds before strong growth begins at after approximately 600 seconds, this time reaching completion after a period of ca. 1300 seconds. In contrast, the corresponding *ex situ* laboratory synthesis carried out at this temperature over a period of 48 hours affords a mixture of phases **1** and **2**, with d-spacings of 9.14 and 9.34 \AA respectively, suggesting that **1** would appear in the *in situ* reaction if left for a longer period of time.

Kinetic parameters were extracted by integration of the Bragg reflection corresponding to $d = 9.4 \text{ \AA}$ using a Gaussian peak fitting routine. The integrated intensities can then be converted to reflect the extent of reaction, α . Sharp-Hancock analysis^{23, 35} was performed for this data set over the range $0.1 < \alpha < 1.0$, and is shown in Figure 40. Linear regression allows the calculation of exponent of 2.5 which implies that the system is controlled by phase-boundary growth (n) in 2 dimensions. A rate constant of $1.69 \times 10^{-7} \text{ s}^{-1}$ suggests a comparatively slow rate of reaction, when compared to other hydrothermal syntheses. The crystallisation of ULM-5 proceeded with rate constants of the order $18.0 \times 10^{-3} \text{ s}^{-1}$ to $5.7 \times 10^{-3} \text{ s}^{-1}$ depending on the reaction temperature ($140 - 180^\circ\text{C}$).⁸

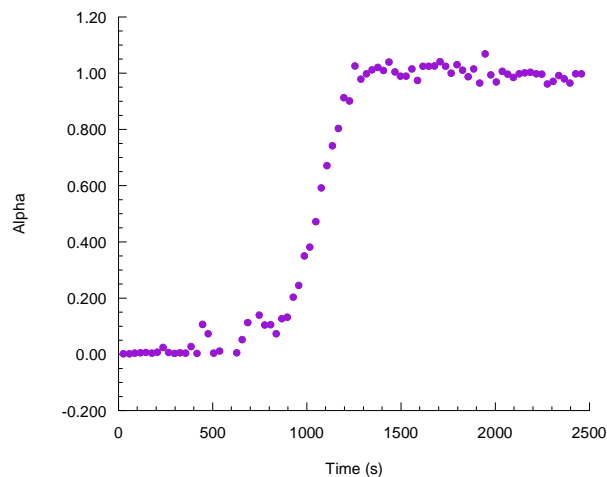


Figure 39 Growth with time of the $d = 9.4 \text{ \AA}$ reflection of $\text{Yb}_2(\text{OH})_5\text{NO}_3 \cdot 2\text{H}_2\text{O}$ (phase 2) synthesised at $100 \text{ }^\circ\text{C}$.

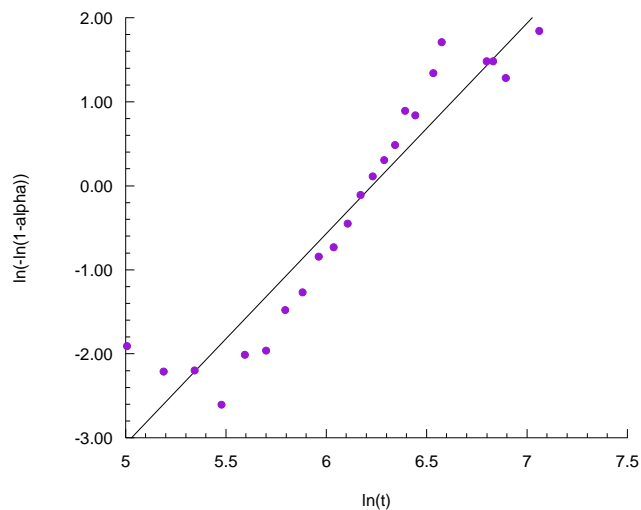


Figure 40 Sharp-Hancock plot of $\ln(-\ln(1-\alpha))$ vs. $\ln t$ for the synthesis of $\text{Yb}_2(\text{OH})_5\text{NO}_3 \cdot 2\text{H}_2\text{O}$ (phase 2) at $100 \text{ }^\circ\text{C}$.

The kinetic parameters obtained from Sharp-Hancock analysis of the reaction as a function of temperature are summarised in Table 8. The induction periods stated refer to the time taken for coherent diffraction for that phase to be observed. The data demonstrate that the induction period for the reaction decreases as the temperature is increased.

Table 8 Kinetic parameters obtained from the Sharp-Hancock analysis of the time resolved *in situ* EDXRD data for **1 - 4**.

Temperature (°C)	Induction Time (s)	Exponent	k (s ⁻¹)
Phase 1: Yb₂(OH)₅NO₃·1.5H₂O (d = 9.2 Å)			
125	570	2.4	3.59 x 10 ⁻⁷
175	270	2.5	9.24 x 10 ⁻⁷
200	270	3.3	1.54 x 10 ⁻⁷
220	90	2.6	1.55 x 10 ⁻⁶
Phase 2: Yb₂(OH)₅NO₃·2H₂O (d = 9.4 Å)			
100	600	2.5	1.69 x 10 ⁻⁷
125	570	1.1	2.40 x 10 ⁻⁶
175	300	1.7	1.07 x 10 ⁻⁵
210	60	2.1	2.44 x 10 ⁻⁵
220	210	1.6	7.15 x 10 ⁻⁵
Phase 3: Yb₂(OH)₅NO₃·H₂O (d = 8.5 Å)			
200	990	2.9	2.38 x 10 ⁻⁷
210	1400	2.0	4.11 x 10 ⁻⁶
Phase 4: Yb₄O(OH)₉NO₃			
210	1950	1.9	5.44 x 10 ⁻⁶

Figure 41 shows the Sharp-Hancock plots for the formation of phase 2 over the temperature range 100 – 220 °C. Validity of the Avrami-Erofe'ev kinetics for this investigation is confirmed by these plots as analysis yields broadly straight lines over the whole reaction. Data for the other phases is included in the Appendices.

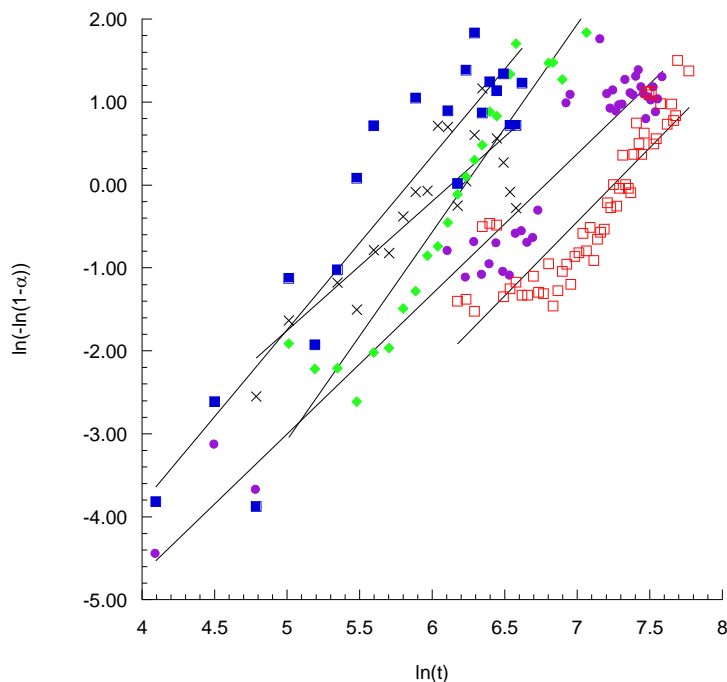


Figure 41 Sharp-Hancock plot of $\ln(-\ln(1-\alpha))$ vs. $\ln t$ for the synthesis of $\text{Yb}_2(\text{OH})_5\text{NO}_3 \cdot 2\text{H}_2\text{O}$ (phase 2) at temperatures 100 – 220 °C. 100 °C (●), 125 °C (□), 175 °C (●), 210 °C (■), 220 °C (x).

The data is fitted with the Avrami-Erofe'ev model and the exponents obtained an average value of $n = 2.5 - 3$ for phase 1 and $n \sim 2$ for phase 2.

For reactions carried out at temperatures over 100 °C kinetic analysis becomes more complex due to the presence of multiple and/or overlapping phases. It is apparent that these reactions occur remarkably quickly, with induction times of less than 300 seconds in some cases. As a result extracted parameters become inherently less reliable due to diminishing numbers of data points in the growth region (less than 10). Due to the

formation of different phases over the temperature ranges, plots of reduced time versus extent of reaction are a more convenient method of comparison. In these plots, reaction time is divided by the half-life of the reaction and can be used to infer whether the mechanism of phase formation is constant under varying conditions.¹⁹ The reduced time plots for each of the phases are super imposable within experimental error, suggesting that each of the phases is formed by a consistent mechanism independent of the reaction conditions applied. Figure 42 shows the reduced time plot for the formation of phase 2, over a range of temperatures 100 – 220 °C with each curve following the same path indicating that the same growth mechanism is followed at each temperature.

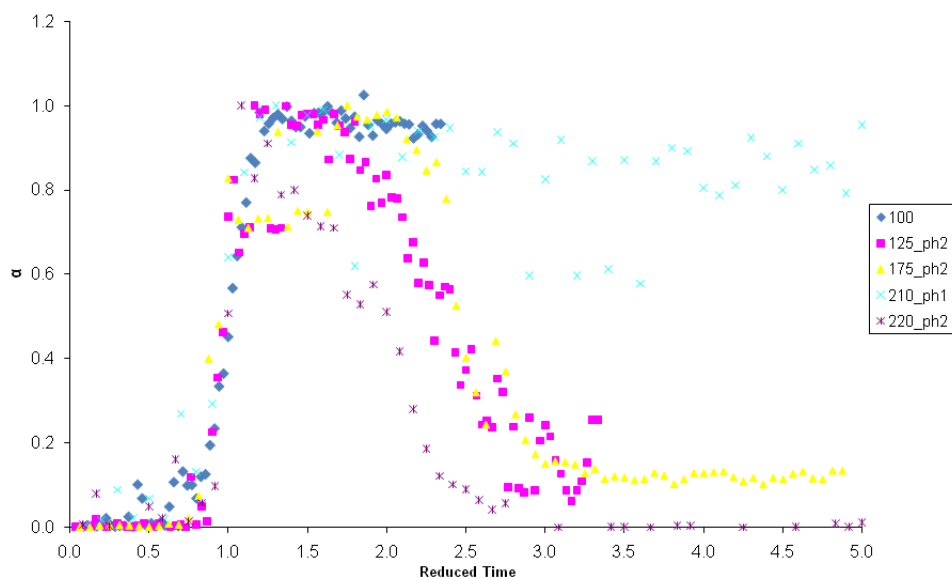


Figure 42 Reduced time plot for $d = 9.4 \text{ \AA}$ phase (2).

Additionally, the rate constants obtained (Table 8) have been used to give an activation energy for the formation of phase **2** using the Arrhenius equation;

$$k = A \exp\left(\frac{-E_a}{RT}\right)$$

Equation 8

A plot of $\ln k$ against $1/T$, shown in Figure 43, allows the activation energy for the formation of phase **2** to be calculated as $+61 \text{ kJ mol}^{-1}$. This is comparable with activation energies observed in other kinetic studies into the liquid phase reconstruction of LDHs and intercalation into layered dichalcogenides of $+41 \text{ kJ mol}^{-1}$,^{7, 24} and the intercalation of Li^+ into gibbsite ($+27 \text{ kJ mol}^{-1}$).¹⁹

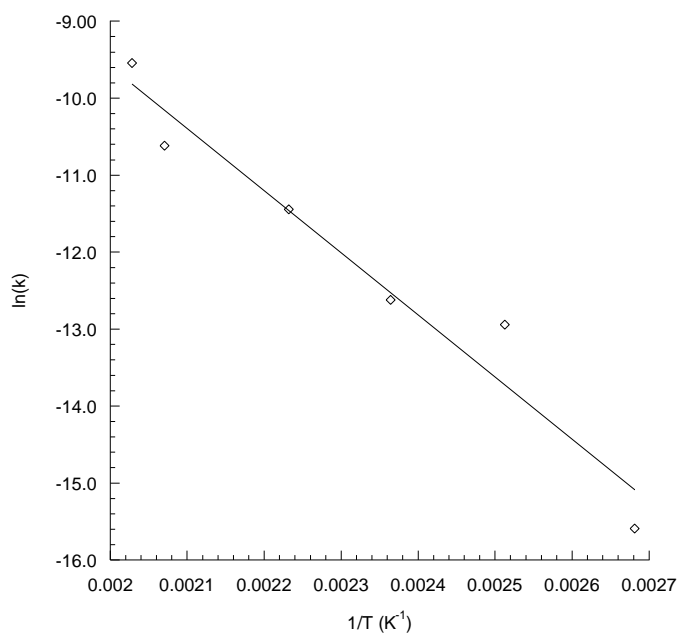


Figure 43 Plot of $\ln(k)$ against $1/T$ for the formation of phase **2**.

The reduced time plots for phases **1** and **3** are shown in Figures 44 and 45 respectively. As for phase **2**, these plots are super imposable within experimental error, supporting the

assertion that each of the phases is formed by a consistent mechanism independent of the reaction temperature.

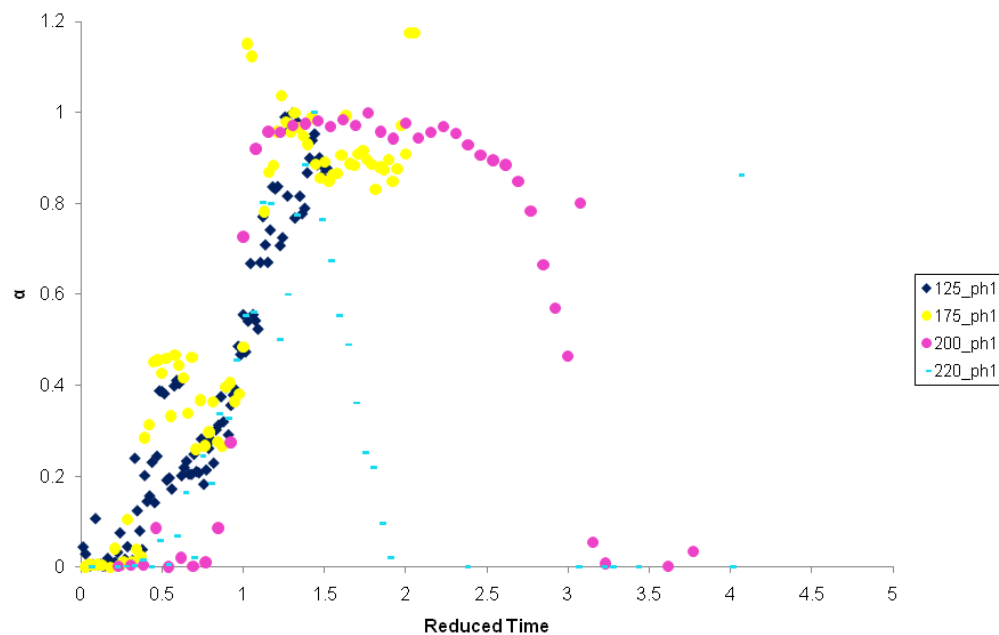


Figure 44 Reduced time plot for $d = 9.2 \text{ \AA}$ phase (1).

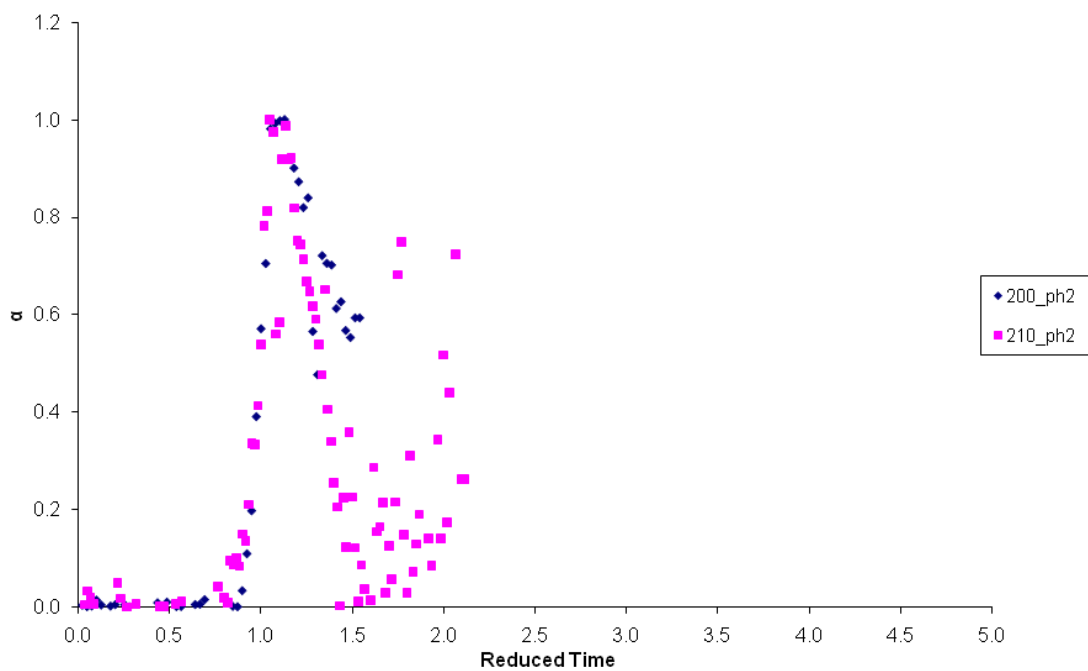


Figure 45 Reduced time plot for $d = 8.5 \text{ \AA}$ phase (3).

3.8.2 Yb concentration experiments

To ascertain the effects of Yb^{3+} concentration on the synthesis of phases **1** - **4** reactions were carried out at concentrations between 0.20 – 0.50 M whilst retaining the standard reaction temperature (150 °C) and NaOH concentration of 2.10 M, The results for both *in situ* and *ex situ* reactions are summarised below in Table 9.

Table 9 Kinetic data for Yb concentration experiments.

Yb ³⁺ Conc (M)	d - spacing (Å)		Induction time (s)	Exponent	k (s ⁻¹)
	<i>Ex situ</i> ^a	<i>In situ</i>			
0.20	9.50, 9.22	9.24	360	2.4	1.19 x 10 ⁻⁶
0.40	9.41, 9.26,	9.49	390	4.4	1.33 x 10 ⁻¹⁰
0.50	9.39, 9.15	9.48	390	3.4	4.12 x 10 ⁻⁸

^a *Ex situ* experiments were carried out for a period of 48 hours.

At Yb^{3+} concentrations lower than 0.33 M, *in situ* experiments show the presence of phase **1** (d ~ 9.2 Å) and at concentrations 0.40 - 0.50 M phase **2** (d ~ 9.4 Å) is observed. Further investigation through *ex situ* experiments under these conditions yielded a mixture of phase **1** and phase **2**. Reactions were carried out at Yb^{3+} concentrations up to 1.0 M with progressively weaker diffraction observed as metal concentration was increased, reflecting a limiting Yb^{3+} concentration with respect to hydroxide for phase formation of 0.20 – 0.50 M. Notably, the induction times for the reactions increase with increasing metal concentration but remain extremely quick at less than 390 seconds. Owing to the extremely weak diffraction observed for *in situ* experiments at Yb^{3+} concentrations of between 0.6 – 1.0 M, the quality of data precluded the calculation of

kinetic parameters. *Ex situ* experiments under these same conditions yield phase **2**. Figure 46 shows the alpha versus time plot for the formation of phase **1** at Yb^{3+} concentration 0.20 M with an induction time of 360 seconds. Sharp-Hancock analysis for this phase (Figure 47) reveals a rate constant, $k = 1.19 \times 10^{-6} \text{ s}^{-1}$ and exponent, $n = 2.4$.

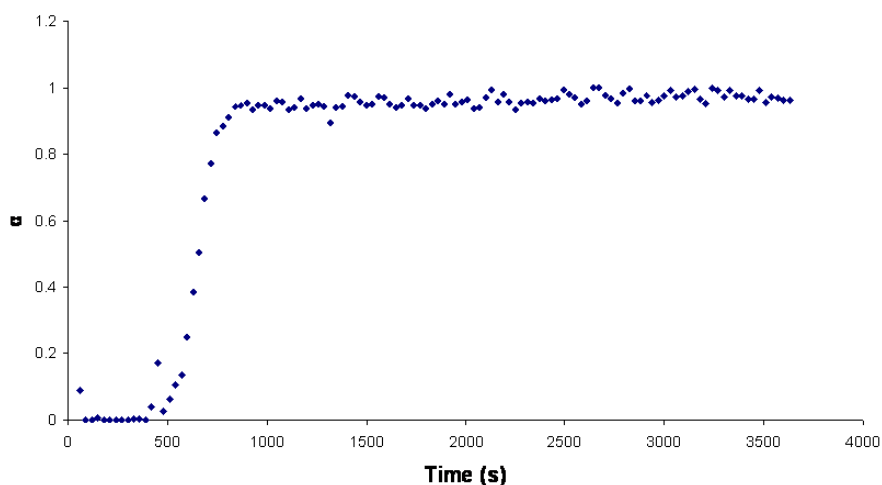


Figure 46 Growth with time of the $d = 9.2 \text{ \AA}$ reflection of $\text{Yb}_2(\text{OH})_5\text{NO}_3 \cdot 1.5\text{H}_2\text{O}$ (phase **1**) synthesised at Yb^{3+} concentration 0.20 M.

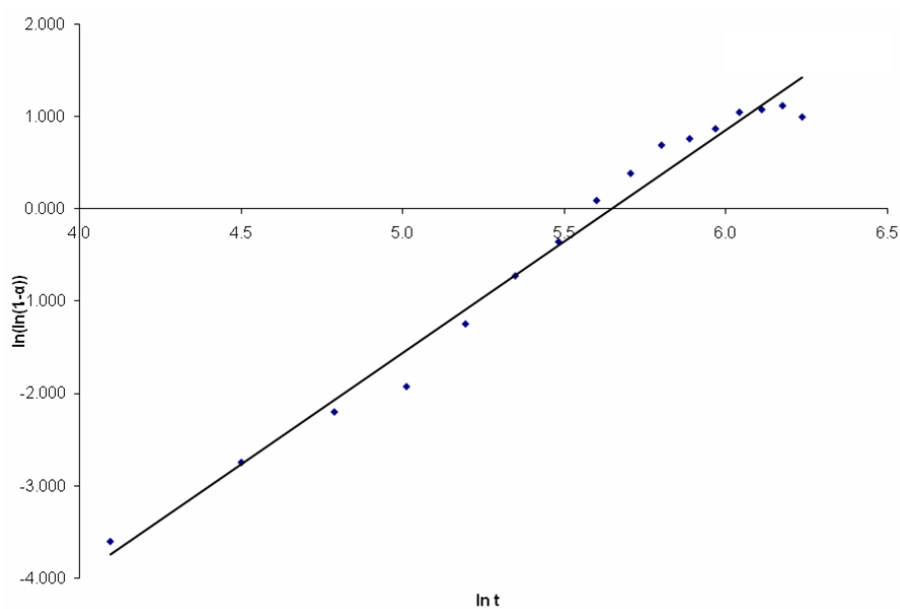


Figure 47 Sharp-Hancock plot of $\ln(-\ln(1-\alpha))$ vs. $\ln t$ for the synthesis of $\text{Yb}_2(\text{OH})_5\text{NO}_3 \cdot 1.5\text{H}_2\text{O}$ (phase **1**) at Yb^{3+} concentration 0.20 M.

Reduced time plots for the formation of phase 2 at metal concentrations 0.40 M and 0.50 M are shown in Figure 48. The curves are super imposable within experimental error indicating that the mechanism for the formation of this phase is the same at both concentrations. Sharp-Hancock analysis for this phase (Figure 49) indicates that at 0.40 M, $n = 4.4$ and $k = 1.33 \times 10^{-10} \text{ s}^{-1}$ whilst at the slightly higher concentration of 0.50 M, $n = 3.4$ with $k = 4.12 \times 10^{-8} \text{ s}^{-1}$. Notably however, there are few data points in the growth region due to the quick formation of the phase which may account for this disparity.

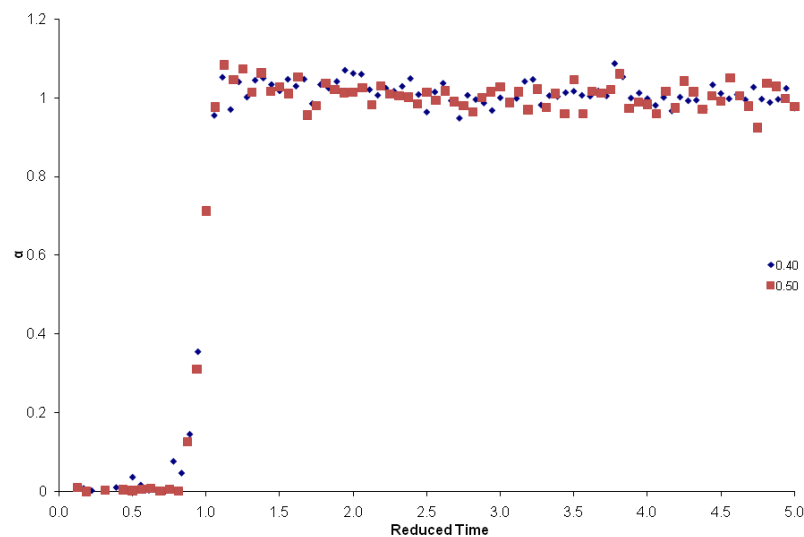


Figure 48 Growth with time of the $d = 9.4 \text{ \AA}$ reflection of $\text{Yb}_2(\text{OH})_5\text{NO}_3 \cdot 2\text{H}_2\text{O}$ (phase 2) synthesised at Yb^{3+} concentrations 0.40 – 0.50 M.

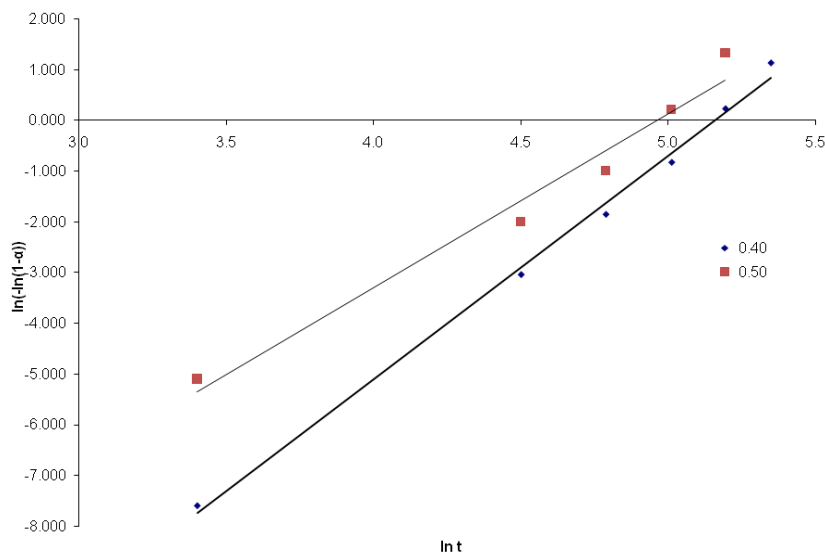


Figure 49 Sharp-Hancock plot of $\ln(-\ln(1-\alpha))$ vs. $\ln t$ for the synthesis of $\text{Yb}_2(\text{OH})_5\text{NO}_3 \cdot 2\text{H}_2\text{O}$ (phase 2) synthesised at Yb^{3+} concentrations 0.40 – 0.50 M.

3.9 Conclusions

Time-resolved *in situ* energy dispersive powder X-ray diffraction has revealed three different phases with the layer composition $[\text{Yb}_2(\text{OH})_5]^+$: $\text{Yb}_2(\text{OH})_5\text{NO}_3 \cdot 1.5\text{H}_2\text{O}$ $d = 9.2$ Å (**1**), $\text{Yb}_2(\text{OH})_5\text{NO}_3 \cdot 2\text{H}_2\text{O}$ $d = 9.4$ Å (**2**) and $\text{Yb}_2(\text{OH})_5\text{NO}_3 \cdot \text{H}_2\text{O}$ $d = 8.5$ Å (**3**), which ultimately all transform to a three-dimensional structure with $d = 8.0$ Å, $\text{Yb}_4\text{O}(\text{OH})_9\text{NO}_3$ (**4**). Progress of the reactions was monitored in real time under hydrothermal conditions and structural transformations between the four phases were observed over a range of temperatures and ytterbium concentrations. Each of these phases have been isolated and the crystal structures of **2**, **3** and **4** are reported. These phases have been fully characterised and their anion exchange properties investigated.

Typically the exponent values for phases **1** – **3** is $n \sim 3$ indicating growth of these materials is phase boundary controlled with a constant nucleation rate. Reduced time plots reveal that the mechanism of formation of each phase is consistent, independent of reaction conditions. The quality of the data was such that kinetic parameters for the formation of phase **2** at 100 °C were able to be extracted, with a rate constant of $1.69 \times 10^{-7} \text{ s}^{-1}$. Further, an Arrhenius plot was used to extract a value for the activation energy for the formation of phase **2** of $+61 \text{ kJ mol}^{-1}$.

The results outlined in this chapter demonstrate the complexities of hydrothermal synthesis and the utility of the EDXRD technique in the resolution of the determining factors involved. In addition, the use of synchrotron radiation in the elucidation of structures from extremely small crystals with relatively high levels of interlayer disorder is illustrated.

3.10 References

1. J. M. Haschke, *Inorganic Chemistry*, 1974, **13**, 1812-1818.
2. I. Schildermans, J. Mullens, J. Yperman, D. Franco and L. C. Vanpoucke, *Thermochimica Acta*, 1994, **231**, 185-192.
3. B. C. Giessen and G. E. Gordon, *Science*, 1968, **159**, 973-&.
4. G. R. Williams, A. I. Khan and D. O'Hare, in *Layered Double Hydroxides*, eds. X. Duan and D. G. Evans, Springer, Berlin, 2006, pp. 161-192.
5. S. M. Clark, A. Nield, T. Rathbone, J. Flaherty, C. C. Tang, J. S. O. Evans, R. J. Francis and D. O'Hare, in *1st European Conference on Synchrotron Radiation in Materials Science*, Chester, England, 1994, pp. 98-101.
6. A. M. Fogg, J. S. Dunn and D. O'Hare, *Chemistry of Materials*, 1998, **10**, 356-360.
7. J. S. O. Evans, S. J. Price, H. V. Wong and D. O'Hare, *Journal of the American Chemical Society*, 1998, **120**, 10837-10846.
8. R. J. Francis, S. O'Brien, A. M. Fogg, P. S. Halasyamani, D. O'Hare, T. Loiseau and G. Ferey, *Journal of the American Chemical Society*, 1999, **121**, 1002-1015.
9. S. M. Clark, *Nuclear Instruments and Methods in Physics Research A*, 1989, **276**, 381-387.
10. S. M. Clark, R. J. Cernik, A. Grant, S. York, P. A. Atkinson, A. Gallagher, D. G. Stokes, S. R. Gregory, N. Harris, W. Smith, M. Hancock, M. C. Miller, K. Ackroyd, R. Farrow, R. Frances and D. O'Hare, *European Powder Diffraction: Epidic Iv, Pts 1 and 2*, 1996, **228**, 213-217.
11. S. M. Clark, J. S. O. Evans, D. O'Hare, C. J. Nuttall and H. V. Wong, *Journal of the Chemical Society-Chemical Communications*, 1994, 809-810.
12. S. M. Clark, A. Nield, T. Rathbone, J. Flaherty, C. C. Tang, J. S. O. Evans, R. J. Francis and D. O'Hare, *Nuclear Instruments & Methods in Physics Research Section B-Beam Interactions with Materials and Atoms*, 1995, **97**, 98-101.
13. G. R. Williams, A. J. Norquist and D. O'Hare, *Chemistry of Materials*, 2004, **16**, 975-981.

14. J. H. Sharp, G. W. Brindley and B. N. Narahariachar, *Journal of the American Ceramic Society*, 1966, **49**, 379-382.
15. M. Avrami, *Journal of Chemical Physics*, 1939, **7**, 1103-1112.
16. M. Avrami, *Journal of Chemical Physics*, 1940, **8**, 212.
17. M. Avrami, *Journal of Chemical Physics*, 1941, **9**, 177-184.
18. B. V. Erofe'ev, *C. R. Doklady Akademii Nauk Sssr*, 1946, **52**, 511.
19. A. M. Fogg and D. O'Hare, *Chemistry of Materials*, 1999, **11**, 1771-1775.
20. A. K. Sheridan and J. Anwar, *Chemistry of Materials*, 1996, **8**, 1042-1051.
21. R. I. Walton, F. Millange, D. O'Hare, A. T. Davies, G. Sankar and C. R. A. Catlow, *Journal of Physical Chemistry B*, 2001, **105**, 83-90.
22. S. F. Hulbert, *Journal of the British Ceramic Society*, 1969, **6**, 11-&.
23. J. D. Hancock and J. H. Sharp, *Journal of the American Ceramic Society*, 1972, **55**, 74-77.
24. F. Millange, R. I. Walton and D. O'Hare, *Journal of Materials Chemistry*, 2000, **10**, 1713-1720.
25. R. J. Francis, S. J. Price, S. O'Brien, A. M. Fogg, D. O'Hare, T. Loiseau and G. Ferey, *Chemical Communications*, 1997, 521-522.
26. R. I. Walton, T. Loiseau, D. O'Hare and G. Ferey, *Chemistry of Materials*, 1999, **11**.
27. F. Millange, R. I. Walton, N. Guillou, T. Loiseau, D. O'Hare and G. Ferey, *Chemical Communications*, 2002, 826-827.
28. F. Millange, R. I. Walton, N. Guillou, T. Loiseau, D. O'Hare and G. Ferey, *Chemistry of Materials*, 2002, **14**, 4448-4459.
29. S. O'Brien, R. J. Francis, S. J. Price, D. O'Hare, S. M. Clark, N. Okazaki and K. Kuroda, *Journal of the Chemical Society-Chemical Communications*, 1995, 2423-2424.
30. S. O'Brien, R. J. Francis, A. Fogg, D. O'Hare, N. Okazaki and K. Kuroda, *Chemistry of Materials*, 1999, **11**, 1822-1832.
31. A. L. Spek, *Journal of Applied Crystallography*, 2003, **36**, 7-13.
32. S. P. Newman and W. Jones, *Journal of Solid State Chemistry*, 1999, **148**, 26-40.

33. A. N. Christensen, M. Nielsen, K. P. J. O'Reilly and T. Wroblewski, *Acta Chemica Scandinavica*, 1992, **46**, 224-230.
34. H. A. Wolcott, W. O. Milligan and G. W. Beall, *Journal of Inorganic & Nuclear Chemistry*, 1977, **39**, 59-63.
35. J. H. Sharp, G. W. Brindley and B. N. N. Achar, *Journal of the American Ceramic Society*, 1966, **49**, 379-&.